Comput Geosci (2016) 20:317–339
DOI 10.1007/s10596-016-9558-3

ORIGINAL PAPER

Model reduction and discretization using hybrid finite volumes for flow in porous media containing faults

Isabelle Faille[1] · Alessio Fumagalli[1] · Jérôme Jaffré[2] · Jean E. Roberts[2]

Received: 13 April 2015 / Accepted: 11 January 2016 / Published online: 11 March 2016

Abstract In this paper, we study two different model reduction strategies for solving problems involving single phase flow in a porous medium containing faults or fractures whose location and properties are known. These faults are represented as interfaces of dimension $N-1$ immersed in an N dimensional domain. Both approaches can handle various configurations of position and permeability of the faults, and one can handle different fracture permeabilities on the two inner sides of the fracture. For the numerical discretization, we use the hybrid finite volume scheme as it is known to be well suited to simulating subsurface flow. Some results, which may be of use in the implementation of the proposed methods in industrial codes, are demonstrated.

Keywords Porous media · Faults · Interface model · Non-matching grids · Finite volumes

✉ Isabelle Faille
isabelle.faille@ifpen.fr

Alessio Fumagalli
alessio.fumagalli1984@gmail.com

Jérôme Jaffré
jerome.jaffre@inria.fr

Jean E. Roberts
jean.roberts@inria.fr

[1] IFP Energies nouvelles, 1 et 4 avenue de Bois-Préau, 92852 Rueil-Malmaison, France

[2] INRIA Roquencourt, BP 105, 78153 Le Chesnay, France

1 Introduction

Fluid flow in porous media can be strongly influenced by the presence of large faults, which, depending on their porosity and permeability, may act as preferential paths for flow linking geologically otherwise unconnected layers or as barriers isolating some part of the fluid. The faults may connect different parts of the domain, and they may also intersect one another. Among the many domains of application requiring an accurate description of fluid flow in faulted media, we mention CO_2 injection and sequestration, oil migration and recovery, and prevention of groundwater contamination from underground nuclear waste disposal, to cite just a few.

Since the width of a fault is several orders of magnitude smaller than any other characteristic size of the porous medium in which it lies and since it is usually very small in comparison to the typical mesh size, it is unreasonable and often for real cases completely unaffordable to uniformly refine the computational grid to a degree that the fault may be represented exactly. To deal with this difficulty, we consider approximation based on a reduced model (RM) in which flow along and across the fracture is described using a simplified set of equations. A reduced model for Darcy flow was introduced in [4] and extended in [18, 34]. In these references, the authors propose a reduced model in which each fault is represented by a single $(N-1)$ dimensional object and flow in the fault is coupled with flow in the rest of the domain by suitable interface conditions. In this article, we will refer to such a model as a *single layer-reduced model* (SLRM) or simply (SL). In the aforementioned works, it was essentially supposed that the fault crossed the entire domain, so, to take into account fractures terminating in the interior of the domain, in [5], the authors extended the model by imposing no flow conditions on the tips of the

faults lying in the interior of the domain. These models were all concerned with single phase Darcy flow. Other results considering similar single-layer reduced models for single phase Darcy flow include [6, 10, 25, 27–29, 31, 32, 36, 37] to name a few.

The SLRM has also been extended to treat nonlinear problems: in [22, 33], an extension was given that couples Forchheimer flow in the fracture with Darcy flow in the surrounding rock matrix. In [30], the authors extended the reduced model to treat a two-phase flow problem by introducing new non-linear coupling conditions for the saturation, which involve the capillary pressure, at the fault interface. Other authors have also treated the case of two-phase flow; we cite [11, 23, 35, 39] among others.

Other types of models for flow in fractured porous media can be found in the literature; see for instance [2, 3, 8, 9].

For the numerical discretization of these reduced models, both finite element and finite volume methods have been analyzed and used effectively showing the flexibility of the models with respect to discretization method. In [21], it was shown that for the numerical discretization of the SLRM, the mesh on one side of the fracture does not need to match up with that on the other nor with the mesh inside the interface fracture. In [13, 20, 24], the authors went further and showed that by using extended finite elements, the mesh on the rock matrix can be chosen completely independently of the fracture, allowing the fracture to cut across cells of the grid.

One application that particularly concerns us here is the simulation of sedimentary basins. In such basins, due to subsurface movements on a geological time scale, the surrounding porous medium on one side of a fault may slip with respect to that on the other. An example is depicted in Fig. 1, where the right side of the domain has slipped with respect to the left side.

To better deal with the case of slipping faults, in [42], the authors extended the reduced model in such a way that each fault is approximated by two distinct $(N-1)$-dimensional objects, one associated with each side of the fault. In the sequel, we will refer to this type of approximation as a *double-layer reduced model* (DLRM) or (DL).

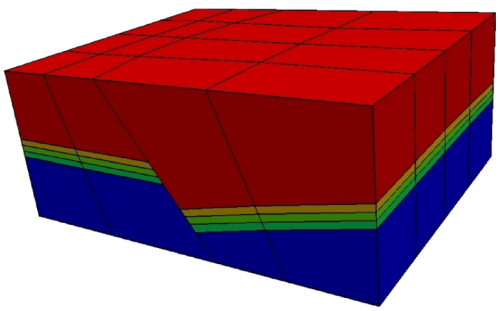

Fig. 1 Example of a schematic basin with slippage along a fault

The main purpose of this article is to give a numerical discretization of the model proposed in [42] using the hybrid finite volume scheme [16, 17] modified to handle the fault flow. A comparison of the SLRM and the DLRM is given in the continuous as well as numerical context, showing their equivalence under suitable conditions. Moreover for both the reduced models, SLRM or DLRM, we prove an equivalence between their numerical approximation and what we call the "virtual fault cell" approach, avoiding the construction of the tangential operators. Several numerical examples are presented to show the robustness of the proposed method for both academic and realistic problems.

The paper is organized as follows: in Section 2, the notation and the governing equations of the physical problem are presented. In Section 3, the double-layer reduced model and the single-layer reduced model are derived and compared. Section 4 is devoted to the discretization of the proposed schemes, and some theoretical results, which may facilitate the implementation, are presented. In Section 5, a collection of examples highlights the possibilities of the proposed methods. Section 6 contains the conclusions. An Appendix A, in which we briefly recall the derivation of the hybrid finite volume scheme for a standard diffusion problem, is included.

2 Flow in a domain with a fault

Throughout the rest of this article, unless otherwise specified, i, respectively j, will denote an index with values $i \in \{1, 2, f\}$, respectively $j \in \{1, 2\}$.

We consider as a computational domain a bounded, connected, open set $\Omega \subset \mathbb{R}^N$, $N = 2$ or 3, representing a porous medium.

We assume that Ω contains a fault Ω_f, a connected, open subset of Ω,and that $\Omega \setminus \overline{\Omega_f}$ is divided into two disjoint, connected, open subsets Ω_j as is shown in Fig. 2. We denote by Γ the boundary of Ω, i.e., $\Gamma := \overline{\Omega} \setminus \Omega$, and by Γ_i the external boundary of Ω_i, i.e., $\Gamma_i := \partial\Omega_i \cap \Gamma$.

The interface between the domain Ω_j and Ω_f is denoted by γ_j and the unit normal vector field on γ_j pointing outward from Ω_j is denoted by $\boldsymbol{n}_j$. We suppose that the fault has a central axis $\hat{\gamma}$, a non self-intersecting $(N-1)$-dimensional surface, such that

$$\Omega_f = \left\{ x \in \mathbb{R}^N : \boldsymbol{x} = \boldsymbol{s} + r\boldsymbol{n},\ \boldsymbol{s} \in \hat{\gamma},\ |r| < \frac{d}{2} \right\},$$

where d is the thickness of Ω_f and $\boldsymbol{n}$ is the continuous unit normal vector field on $\hat{\gamma}$, pointing outward from Ω_1 toward Ω_2. We assume that the thickness d of Ω_f is negligible compared to its other dimensions.

Throughout the following, we indicate with a subscript i, or j as appropriate, the restriction of data and unknown

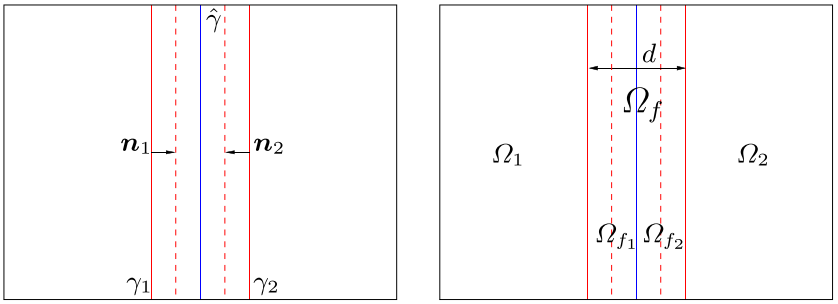

Fig. 2 Representation of each sub-domain

functions (scalar or vector) to the corresponding subdomain of Ω.

Our purpose is to compute the steady pressure field p and the velocity field, or Darcy velocity, $\boldsymbol{u}$ in the entire domain Ω. We suppose that flow is governed by the law of mass conservation together with Darcy's law, and for simplicity, we assume that the only boundary condition on Γ is a homogeneous condition for the pressure:

$$\begin{aligned} &\nabla \cdot \boldsymbol{u} = q \\ &\boldsymbol{u} + \Lambda \nabla p = \boldsymbol{0} \quad \text{in } \Omega \\ &p = 0 \quad \text{on } \Gamma. \end{aligned} \tag{1}$$

Here, Λ denotes the symmetric and positive definite permeability tensor in Ω, and the scalar source term q represents a possible volume source or sink. We write problem (1) as an equivalent transmission problem:

$$\begin{aligned} &\nabla \cdot \boldsymbol{u}_i = q_i \\ &\boldsymbol{u}_i + \Lambda_i \nabla p_i = \boldsymbol{0} \quad \text{in } \Omega_i \\ &p_i = 0 \quad \text{on } \Gamma_i, \end{aligned} \tag{2a}$$

coupled with interface conditions:

$$\begin{aligned} &p_j = p_f \\ &\boldsymbol{u}_j \cdot \boldsymbol{n}_j = \boldsymbol{u}_f \cdot \boldsymbol{n}_j \quad \text{on } \gamma_j. \end{aligned} \tag{2b}$$

We have supposed, following [34], that the permeability tensor in Ω_f can be written as $\Lambda_f = \lambda_{f,\boldsymbol{n}} \boldsymbol{N} + \lambda_{f,\boldsymbol{\tau}} \boldsymbol{T}$, where the projection matrix $\boldsymbol{N}$ in the direction normal to $\hat{\gamma}$ and the projection matrix $\boldsymbol{T}$ in the direction tangential to $\hat{\gamma}$ are defined as follows:

$$\boldsymbol{N} := \boldsymbol{n} \otimes \boldsymbol{n} \quad \text{and} \quad \boldsymbol{T} := \boldsymbol{I} - \boldsymbol{N}.$$

The demonstration of the well posedness of problem (1) in its mixed weak form can be found in any number of texts; see [12, 15, 38, 41].

3 A double-layer reduced model

We are interested in a reduced model in which the fault Ω_f is represented by an interface which is identified with its central axis $\hat{\gamma}$. However, since Ω_1 can slip along the fault with respect to Ω_2, or vice versa, following [42], we subdivide Ω_f into two disjoint layers Ω_{f_j}, such that $\overline{\Omega_f} = \cup_j \overline{\Omega_{f_j}}$:

$$\Omega_{f_j} = \left\{ \boldsymbol{x} \in \mathbb{R}^N : \boldsymbol{x} = \boldsymbol{s} + r\boldsymbol{n},\ \boldsymbol{s} \in \hat{\gamma},\ r \in T_j \right\},$$

where $T_1 = (-d/2, 0)$ and $T_2 = (0, d/2)$. Each layer Ω_{f_j}, in turn has a central axis, a translation of $\hat{\gamma}$, which we denote by $\hat{\gamma}_j$. For a double-layer reduced model, a DLRM, each layer Ω_{f_j} is approximated by its central axis $\hat{\gamma}_j$. We first derive equations governing flow in $\hat{\gamma}_j$ and an equation coupling flow in $\hat{\gamma}_j$ with flow in Ω_j. These equations are derived similarly to the corresponding equations in the single-layer reduced model, the SLRM. Then to complete the model, we derive an equation coupling flow in $\hat{\gamma}_1$ with flow in $\hat{\gamma}_2$, as in the final model $\hat{\gamma}$, $\hat{\gamma}_1$, and $\hat{\gamma}_2$ are all identified with each other. Also in the final model, after the reductions process, it is implicitly supposed that the surrounding porous medium is extended to the fault line. However, this is not taken into account in the model as the fracture is assumed to be narrow enough that the effect of such an extension would be negligible

3.1 Derivation of the DLRM

To obtain the equations describing flow on $\hat{\gamma}_j$, we integrate the equations for flow in Ω_f, Eq. 2a, across normal cross sections of Ω_{f_j}. However, we first split the vector terms into their normal and tangential parts. To do this, we will make use of the normal and tangential divergence and gradient operators:

$$\begin{aligned} &\nabla_{\boldsymbol{n}} \cdot := \boldsymbol{N} : \nabla \quad \text{and} \quad \nabla_{\boldsymbol{\tau}} \cdot := \boldsymbol{T} : \nabla, \\ &\nabla_{\boldsymbol{n}} := \boldsymbol{N} \nabla \quad \text{and} \quad \nabla_{\boldsymbol{\tau}} := \boldsymbol{T} \nabla, \end{aligned}$$

and we will write the Darcy velocity in Ω_f as a sum of its normal and tangential components:

$$\boldsymbol{u}_f = \boldsymbol{N}\boldsymbol{u}_f + \boldsymbol{T}\boldsymbol{u}_f = \boldsymbol{u}_{f,n} + \boldsymbol{u}_{f,\boldsymbol{\tau}}$$

with $\boldsymbol{u}_{f,\boldsymbol{n}} := \boldsymbol{N}\boldsymbol{u}_f$ and $\boldsymbol{u}_{f,\boldsymbol{\tau}} := \boldsymbol{T}\boldsymbol{u}_f$. We will use the hat notation $\hat{\cdot}$ to denote reduced functions, i.e., functions defined on $\hat{\gamma}_1$ or $\hat{\gamma}_2$ in the reduced model. The reduced source term on $\hat{\gamma}_j$ is defined to be $\hat{q}_j := \int_{T_j} q_f$, while the reduced (tangential) Darcy velocity along $\hat{\gamma}_j$ is $\hat{\boldsymbol{u}}_{\boldsymbol{j}} := \int_{T_j} \boldsymbol{u}_{f,\boldsymbol{\tau}}$. Then integrating the conservation equation, the

second equation of Eq. 2a, across normal cross sections of Ω_{f_j} we obtain

$$\int_{T_j} \nabla \cdot \boldsymbol{u}_f = \boldsymbol{u}_f \cdot \boldsymbol{n}\big|_{\hat{\gamma}} - \boldsymbol{u}_f \cdot \boldsymbol{n}\big|_{\gamma_j} + \nabla_{\boldsymbol{\tau}} \cdot \hat{\boldsymbol{u}}_j = \hat{q}_j$$

which we may now write as

$$\nabla_{\boldsymbol{\tau}} \cdot \hat{\boldsymbol{u}}_j = \hat{q}_j + [\![\boldsymbol{u} \cdot \boldsymbol{n}]\!]_{\gamma_j} \quad \text{in } \hat{\gamma}_j, \tag{3}$$

where we have introduced the flux jump $[\![\boldsymbol{u} \cdot \boldsymbol{n}]\!]_{\gamma_j}$ across $\hat{\gamma}_j$ defined by

$$\begin{aligned}[\![\boldsymbol{u} \cdot \boldsymbol{n}]\!]_{\gamma_j} &:= (-1)^j (\boldsymbol{u}_f \cdot \boldsymbol{n}\big|_{\hat{\gamma}} - \boldsymbol{u}_f \cdot \boldsymbol{n}\big|_{\gamma_j}) \\ &= (-1)^j \left(\hat{u}_{\boldsymbol{n}} - \boldsymbol{u}_j \cdot \boldsymbol{n}\big|_{\gamma_j}\right).\end{aligned}$$

For the second equality, we have used the continuity of the flux at γ_j, the second equation of Eq. 2b, and have introduced the notation $\hat{u}_{\boldsymbol{n}}$ for $\boldsymbol{u}_f \cdot \boldsymbol{n}\big|_{\hat{\gamma}}$.

We consider now Darcy's law in the fault Ω_f and split it into its normal and tangential components:

$$\begin{aligned}\boldsymbol{u}_{f,\boldsymbol{n}} &= -\lambda_{f,\boldsymbol{n}} \nabla_{\boldsymbol{n}} p_f \\ \boldsymbol{u}_{f,\boldsymbol{\tau}} &= -\lambda_{f,\boldsymbol{\tau}} \nabla_{\boldsymbol{\tau}} p_f.\end{aligned}$$

To derive a reduced form of Darcy's law on $\hat{\gamma}_j$, we will need the reduced pressure $\hat{p}_j$ and the reduced permeability $\hat{\lambda}$ defined by

$$\hat{p}_j := \frac{2}{d} \int_{T_j} p_f \quad \text{and} \quad \hat{\lambda} := d \frac{\lambda_{f,\boldsymbol{\tau}}}{2}.$$

Considering the tangential part of Darcy's law and integrating it across normal cross sections of each layer of the fault we obtain

$$\hat{\boldsymbol{u}}_j = -\hat{\lambda} \nabla_{\boldsymbol{\tau}} \hat{p}_j, \quad \text{in } \hat{\gamma}_j. \tag{4}$$

The normal part of Darcy's law can now be used to derive a condition coupling flow in $\hat{\gamma}_j$ with flow in Ω_j. We integrate over the normal cross sections of the outer half of the layer Ω_{f_j} and use the first equation of Eq. 2b, the continuity condition for the pressure at the interface γ_j,to obtain

$$\int_a^b \boldsymbol{u}_{f,\boldsymbol{n}} \cdot \boldsymbol{n} = (-1)^j \lambda_{f,\boldsymbol{n}} \left(\hat{p}_j - p_j\right),$$

where a and b are, respectively, $-\frac{d}{2}$ and $-\frac{d}{4}$ if $j = 1$ and $\frac{d}{4}$ and $\frac{d}{2}$ if $j = 2$. Approximating the integral in the preceding equation as follows:

$$\int_a^b \boldsymbol{u}_{f,\boldsymbol{n}} \cdot \boldsymbol{n} \approx \frac{d}{4} \boldsymbol{u}_{f,\boldsymbol{n}} \cdot \boldsymbol{n}\big|_{\gamma_j},$$

and using the continuity condition for the normal component of the velocity, the second equation of Eq. 2b, we obtain the coupling condition

$$\boldsymbol{u}_j \cdot \boldsymbol{n} = (-1)^j 2\hat{\lambda}_{\boldsymbol{n}} \left(\hat{p}_j - p_j\right), \quad \text{on } \hat{\gamma}_j, \tag{5}$$

where $\hat{\lambda}_{\boldsymbol{n}} := \frac{2}{d} \lambda_{f,\boldsymbol{n}}$.

Now, even though $\hat{\gamma}_j$ and $\hat{\gamma}$ are, in the DLRM, in fact the same interface, they are thought of as being different sides of the interface, and two distinct flows (Darcy velocities and pressures) $(\hat{\boldsymbol{u}}_j, \hat{p}_j)$ are calculated, so an additional equation is now needed to express the coupling between the two sides of the fault. To obtain this, we consider again the normal component of the Darcy equation in Ω_f and this time integrate across the normal cross sections of the inner halves of the two layers Ω_{f_1} and Ω_{f_2}:

$$\int_{-\frac{d}{4}}^{\frac{d}{4}} \boldsymbol{u}_{f,\boldsymbol{n}} \cdot \boldsymbol{n} = -\lambda_{f,\boldsymbol{n}} \left(\hat{p}_2 - \hat{p}_1\right).$$

Then using a mid-point rule to approximate the integral of $\boldsymbol{u}_{f,\boldsymbol{n}} \cdot \boldsymbol{n}$,

$$\int_{-\frac{d}{4}}^{\frac{d}{4}} \boldsymbol{u}_{f,\boldsymbol{n}} \cdot \boldsymbol{n} \approx \frac{d}{2} \boldsymbol{u}_f \cdot \boldsymbol{n}\big|_{\hat{\gamma}} = \frac{d}{2} \hat{u}_{\boldsymbol{n}},$$

we obtain the condition

$$\hat{u}_{\boldsymbol{n}} = \hat{\lambda}_{\boldsymbol{n}} [\![\hat{p}]\!]_{\hat{\gamma}}, \tag{6}$$

where $[\![\hat{p}]\!]_{\hat{\gamma}} := \hat{p}_1 - \hat{p}_2$.

Collecting the Eq. 2a for flow in Ω_j, Eqs. 3 and 4 for flow in the reduced fault layers $\hat{\gamma}_j$, and the coupling conditions (5) and (6), we obtain the double-layer reduced model: for the porous medium domains Ω_j

$$\begin{aligned}&\nabla \cdot \boldsymbol{u}_j = q_j \\ &\boldsymbol{u}_j = -\Lambda_j \nabla p_j \qquad \text{in } \Omega_j, \\ &p_j = 0 \qquad\qquad \text{on } \Gamma_j\end{aligned} \tag{7a}$$

for the two reduced layers of the fault

$$\begin{aligned}&\nabla_{\boldsymbol{\tau}} \cdot \hat{\boldsymbol{u}}_j = \hat{q}_j + [\![\boldsymbol{u} \cdot \boldsymbol{n}]\!]_{\gamma_j} \\ &\hat{\boldsymbol{u}}_j = -\hat{\lambda} \nabla_{\boldsymbol{\tau}} \hat{p}_j \qquad\qquad \text{in } \hat{\gamma}_j, \\ &\hat{p}_j = 0 \qquad\qquad\quad \text{on } \partial\hat{\gamma}_j\end{aligned} \tag{7b}$$

with the coupling conditions

$$\begin{aligned}&\boldsymbol{u}_1 \cdot \boldsymbol{n} = 2\hat{\lambda}_{\boldsymbol{n}} \left(p_1 - \hat{p}_1\right) \quad \text{on } \hat{\gamma}_1 \\ &\boldsymbol{u}_2 \cdot \boldsymbol{n} = 2\hat{\lambda}_{\boldsymbol{n}} \left(\hat{p}_2 - p_2\right) \quad \text{on } \hat{\gamma}_2 \\ &\hat{u}_{\boldsymbol{n}} = \hat{\lambda}_{\boldsymbol{n}} [\![\hat{p}]\!]_{\hat{\gamma}} \quad\quad \text{on } \hat{\gamma}.\end{aligned} \tag{7c}$$

As mentioned earlier, while constructing the DLRM, we have distinguished three different interfaces, $\hat{\gamma}_1$, $\hat{\gamma}$, and $\hat{\gamma}_2$, which are all in fact in the final model associated with the same interface-domain. An alternative form of (7c) can thus be obtained by considering the three equations to be equations on the same interface $\hat{\gamma}$ and adding and subtracting the first two equations to obtain an equivalent version of the coupling conditions on $\hat{\gamma}$:

$$\begin{aligned}&\{\!\{\boldsymbol{u} \cdot \boldsymbol{n}\}\!\}_{\hat{\gamma}} = \hat{\lambda}_{\boldsymbol{n}} \left([\![p]\!]_{\hat{\gamma}} - [\![\hat{p}]\!]_{\hat{\gamma}}\right) \\ &[\![\boldsymbol{u} \cdot \boldsymbol{n}]\!]_{\hat{\gamma}} = 4\hat{\lambda}_{\boldsymbol{n}} \left(\{\!\{p\}\!\}_{\hat{\gamma}} - \{\!\{\hat{p}\}\!\}_{\hat{\gamma}}\right) \\ &\hat{u}_{\boldsymbol{n}} = \hat{\lambda}_{\boldsymbol{n}} [\![\hat{p}]\!]_{\hat{\gamma}}.\end{aligned} \tag{7c-bis}$$

Here, the mean operators are defined by

$$\{\!\{\boldsymbol{u}\cdot\boldsymbol{n}\}\!\}_{\hat{\gamma}} := \frac{1}{2}\left(\boldsymbol{u}_1\cdot\boldsymbol{n}|_{\hat{\gamma}} + \boldsymbol{u}_2\cdot\boldsymbol{n}|_{\hat{\gamma}}\right)$$
$$\{\!\{p\}\!\}_{\hat{\gamma}} := \frac{1}{2}\left(p_1|_{\hat{\gamma}} + p_2|_{\hat{\gamma}}\right)$$

and the jump operators by

$$[\![\boldsymbol{u}\cdot\boldsymbol{n}]\!]_{\hat{\gamma}} := \boldsymbol{u}_1\cdot\boldsymbol{n}|_{\hat{\gamma}} - \boldsymbol{u}_2\cdot\boldsymbol{n}|_{\hat{\gamma}}$$
$$[\![p]\!]_{\hat{\gamma}} := p_1|_{\hat{\gamma}} - p_2|_{\hat{\gamma}}.$$

Remark 1 We point that one can consider different values of $\hat{\lambda}$ and $\hat{\lambda}_{\boldsymbol{n}}$ for each layer, and this is an important property of the DLRM that the SLRM does not have. However, for simplicity of exposition, we have not done this here. Nonetheless, in Section 5.3, we give an example with different values of $\hat{\lambda}$ each layer of the fault.

3.2 Weak formulation of the DLRM

The numerical discretization that we will use for the approximation of Eq. 7 is based on a weak formulation which we now define. Let $\mathcal{V} := \prod_{j=1}^{2}\mathcal{V}_j$, where $\mathcal{V}_j := H^1_\Gamma(\Omega_j)$ is the space of those functions in $H^1(\Omega_j)$ having a vanishing trace on $\partial\Omega_j \cap \Gamma$ and $\hat{\mathcal{V}} := \prod_{j=1}^{2}\hat{\mathcal{V}}_j$, where $\hat{\mathcal{V}}_j = H^1_\Gamma(\hat{\gamma})$ is the space of functions in $H^1(\hat{\gamma})$ having a vanishing trace on $\partial\hat{\gamma}\cap\Gamma$. We then define the bilinear forms a_Ω and $a_{\hat{\gamma}}$ on $\mathcal{V}\times\mathcal{V}$ and $\hat{\mathcal{V}}\times\hat{\mathcal{V}}$, respectively, by

$$a_\Omega(p,v) := \sum_{j=1,2}\left(\Lambda_j\nabla p_j, \nabla v_j\right)_{\Omega_j}, \tag{8}$$

and

$$a_{\hat{\gamma}}(\hat{p},\hat{v}) := \sum_{j=1,2}\left(\hat{\lambda}\nabla_{\boldsymbol{\tau}}\hat{p}_j, \nabla_{\boldsymbol{\tau}}\hat{v}_j\right)_{\hat{\gamma}_j}, \tag{9}$$

and the global diffusion bilinear form a is defined on $(\mathcal{V}\times\hat{\mathcal{V}})\times(\mathcal{V}\times\hat{\mathcal{V}})$ by

$$a\big((p,\hat{p}),(v,\hat{v})\big) := a_\Omega(p,v) + a_{\hat{\gamma}}(\hat{p},\hat{v}).$$

To enforce the coupling conditions (7c) in the weak formulation, we need another bilinear form. Let cc denote the bilinear form defined on $(\mathcal{V}\times\hat{\mathcal{V}})\times(\mathcal{V}\times\hat{\mathcal{V}})$ by

$$cc\big((p,\hat{p}),(v,\hat{v})\big) := \left(\hat{\lambda}_{\boldsymbol{n}}[\![\hat{p}]\!]_{\hat{\gamma}}, [\![\hat{v}]\!]_{\hat{\gamma}}\right)_{\hat{\gamma}} + \sum_{j=1,2} 2\left(\hat{\lambda}_{\boldsymbol{n}}p_j - \hat{\lambda}_{\boldsymbol{n}}\hat{p}_j, v_j - \hat{v}_j\right)_{\hat{\gamma}_j}, \tag{10}$$

which using Eq. 7c-bis may alternatively be written as

$$cc\big((p,\hat{p}),(v,\hat{v})\big) := \left(\hat{\lambda}_{\boldsymbol{n}}[\![\hat{p}]\!]_{\hat{\gamma}}, [\![\hat{v}]\!]_{\hat{\gamma}}\right)_{\hat{\gamma}} + 4\left(\hat{\lambda}_{\boldsymbol{n}}\{\!\{p\}\!\}_{\hat{\gamma}} - \hat{\lambda}_{\boldsymbol{n}}\{\!\{\hat{p}\}\!\}_{\hat{\gamma}}, \{\!\{v\}\!\}_{\hat{\gamma}} - \{\!\{\hat{v}\}\!\}_{\hat{\gamma}}\right)_{\hat{\gamma}} + \left(\hat{\lambda}_{\boldsymbol{n}}[\![p]\!]_{\hat{\gamma}} - \hat{\lambda}_{\boldsymbol{n}}[\![\hat{p}]\!]_{\hat{\gamma}}, [\![v]\!]_{\hat{\gamma}} - [\![\hat{v}]\!]_{\hat{\gamma}}\right)_{\hat{\gamma}}. \tag{10-bis}$$

The right-hand side functional F is defined on $\mathcal{V}\times\hat{\mathcal{V}}$ by

$$F(v,\hat{v}) := \sum_{j=1,2}(q_j, v_j)_{\Omega_j} + \sum_{j=1,2}(\hat{q}_j,\hat{v}_j)_{\hat{\gamma}_j}.$$

The weak formulation of Eq. 7 may be written as follows:

$$\begin{aligned}&\text{find } (p,\hat{p})\in\mathcal{V}\times\hat{\mathcal{V}} \text{ such that}\\ &a\big((p,\hat{p}),(v,\hat{v})\big) + cc\big((p,\hat{p}),(v,\hat{v})\big) = F(v,\hat{v}),\\ &\text{for all } (v,\hat{v})\in\mathcal{V}\times\hat{\mathcal{V}}.\end{aligned} \tag{11}$$

3.3 Weak formulation of the SLRM

We point out that the SLRM in [13, 34], with a suitable choice of the weighting parameter, can be recovered by requiring that $\hat{p}_1 = \hat{p}_2$, which implies that $\hat{\boldsymbol{u}}_1 = \hat{\boldsymbol{u}}_2$, and that $\hat{u}_{\boldsymbol{n}} = (\boldsymbol{u}_1\cdot\boldsymbol{n} + \boldsymbol{u}_2\cdot\boldsymbol{n})/2 + (\hat{q}_1 - \hat{q}_2)/2$. This, however, is equivalent to collapsing the interior half of the fault resulting in a fault of half the width. Thus to maintain the full width of the fault, every occurrence of d should be replaced by $2d$ or more to the point, every occurrence of $\hat{\lambda}$ by $2\hat{\lambda}$ and every occurrence of $\hat{\lambda}_{\boldsymbol{n}}$ by $\hat{\lambda}_{\boldsymbol{n}}/2$. Thus, now writing $\hat{p}$ for $\hat{p}_j$, $\hat{\boldsymbol{u}}$ for $\hat{\boldsymbol{u}}_1 + \hat{\boldsymbol{u}}_2$ and $\hat{q}$ for $\hat{q}_1 + \hat{q}_2$, the SLRM can be written as follows: for the porous medium domains Ω_j

$$\begin{aligned}&\nabla\cdot\boldsymbol{u}_j = q_j\\ &\boldsymbol{u}_j = -\Lambda_j\nabla p_j \quad \text{in } \Omega_j\\ &p = 0 \quad \text{on } \Gamma_j\end{aligned} \tag{12a}$$

for the the reduced fault $\hat{\gamma}$

$$\begin{aligned}&\nabla_{\boldsymbol{\tau}}\cdot\hat{\boldsymbol{u}} = \hat{q} + [\![\boldsymbol{u}\cdot\boldsymbol{n}]\!]_{\hat{\gamma}}\\ &\hat{\boldsymbol{u}} = -2\hat{\lambda}\nabla_{\boldsymbol{\tau}}\hat{p} \quad \text{in } \hat{\gamma}\\ &\hat{p} = 0 \quad \text{on } \partial\hat{\gamma}\end{aligned} \tag{12b}$$

with the coupling conditions

$$\begin{aligned}&\{\!\{\boldsymbol{u}\cdot\boldsymbol{n}\}\!\}_{\hat{\gamma}} = \frac{\hat{\lambda}_{\boldsymbol{n}}}{2}[\![p]\!]_{\hat{\gamma}}\\ &[\![\boldsymbol{u}\cdot\boldsymbol{n}]\!]_{\hat{\gamma}} = 2\hat{\lambda}_{\boldsymbol{n}}\left(\{\!\{p\}\!\}_{\hat{\gamma}} - \hat{p}\right) \quad \text{on } \hat{\gamma}.\end{aligned} \tag{12c}$$

Note that in the case of the SLRM, the weak formulation of Eq. 7 is modified as follows: the space $\mathcal{V}$ is unchanged, the space $\hat{\mathcal{V}}$ is replaced by a single copy (instead of two) of $H^1_\Gamma(\hat{\gamma})$, in the two bilinear forms making up $a((\cdot,\cdot),(\cdot,\cdot))$ the bilinear form $a_\Omega(\cdot,\cdot)$ is unchanged, and the bilinear

form $a_{\hat{\gamma}}(\cdot,\cdot)$ is modified by removing the sum over j and dropping the index j, and multiplying by 2:

$$a_{\hat{\gamma}}\left(\hat{p},\hat{v}\right) := 2\left(\hat{\lambda}\nabla_{\boldsymbol{\tau}}\hat{p},\nabla_{\boldsymbol{\tau}}\hat{v}\right)_{\hat{\gamma}}. \tag{13}$$

For the SLRM, the bilinear form for the coupling simplifies to

$$cc\big((p,\hat{p}),(v,\hat{v})\big) := \frac{1}{2}\left(\hat{\lambda}_{\boldsymbol{n}}\left[\![p]\!]_{\hat{\gamma}},[\![v]\!]_{\hat{\gamma}}\right)_{\hat{\gamma}} + 2\left(\hat{\lambda}_{\boldsymbol{n}}(\{\!\{p\}\!\}_{\hat{\gamma}}-\hat{p}),(\{\!\{v\}\!\}_{\hat{\gamma}}-\hat{v})\right)_{\hat{\gamma}}. \tag{14}$$

4 Numerical approximation

The numerical approximation of the proposed models is the main part of this work. For the derivation of the approximation, we will consider only planar faults and faces, although some numerical results with non-planar faults are shown in Section 5. In the first subsection, we briefly recall the hybrid finite volume (HFV) scheme which is the basis for the numerical scheme we use, (a more thorough description is given in Appendix A.2) and show how this scheme can be extended to approximate a reduced fault model. Then follows an exposition of approximation using the *virtual fault cells* approach. The final subsection is devoted to a comparison of the two discretization techniques.

4.1 Discretization with the HFV scheme

In this part, we present the numerical discretization of both DLRM and SLRM using the HFV scheme.

4.1.1 Discrete unknowns

To solve numerically (7) and (12), we use the hybrid finite volume (HFV) scheme, introduced in [14, 17]. First, we recall what is meant by an HFV discretization of an open set $\mathcal{O}\subset\mathbb{R}^N$ for $N=1,2,3$.

Notation 1 (Discretization of $\mathcal{O}$) For $\mathcal{O}$ an open set in $\mathbb{R}^N$, a discretization of $\mathcal{O}$, denoted by $\mathcal{D}$ is defined to be a triple $\mathcal{D}:=(\mathcal{M},\mathcal{E},\mathcal{P})$ where

1. $\mathcal{M}$ is a set of cells or control volumes, i.e., a set of disjoint, non-empty, open, polyhedra if $N=3$, polygons if $N=2$, or line segments if $N=1$, lying in $\mathcal{O}$ such that
$$\overline{\mathcal{O}} = \bigcup_{K\in\mathcal{M}}\overline{K}. \tag{15}$$
For K a cell, let $|K|>0$ denote the measure of K.
2. $\mathcal{E}$ is the set of the $(N-1)$-dimensional faces of the cells in $\mathcal{M}$. The set $\mathcal{E}$ is divided into the set of external faces $\mathcal{E}_{\text{ext}}=\{\sigma\in\mathcal{E}: E\subset\partial\mathcal{O}\}$, and the set of internal faces $\mathcal{E}_{\text{int}}=\{\sigma\in\mathcal{E}: E\subset\mathcal{O}\}$. We have $\mathcal{E}=\mathcal{E}_{\text{int}}\cup\mathcal{E}_{\text{ext}}$. For $\sigma\in\mathcal{E}$, $|\sigma|>0$ will denote the measure of σ. We assume $|\sigma|=1$ if $N=1$. For each cell $K\in\mathcal{M}$, we denote by $\mathcal{E}_K\subset\mathcal{E}$ the set of all $(N-1)$-dimensional faces of K and for each face $\sigma\in\mathcal{E}$, we denote by $\mathcal{M}_\sigma:=\{K\in\mathcal{M}: \sigma\in\mathcal{E}_K\}$ the set of all cells in $\mathcal{M}$ having σ as a face;
3. $\mathcal{P}$ is the set of points, defined by $\mathcal{P}:=\{\boldsymbol{x}_K: K\in\mathcal{M}\}\cup\{\boldsymbol{x}_\sigma:\sigma\in\mathcal{E}\}$, where $\boldsymbol{x}_K$ is the barycentre of the cell $K\in\mathcal{M}$ and $\boldsymbol{x}_\sigma$ is the barycentre of the face $\sigma\in\mathcal{E}$;
4. For each cell $K\in\mathcal{M}$ and face $\sigma\in\mathcal{E}_K$, we indicate by $\boldsymbol{n}_{K,\sigma}$ the unit vector normal to σ pointing outward from K. If $N=1$, then $\boldsymbol{n}_{K,\sigma}$ is just the vector tangential to K at σ and pointing outward from K;
5. For each cell $K\in\mathcal{M}$ and face $\sigma\in\mathcal{E}_K$, we denote by $D_{K,\sigma}\subset K$ the cone with vertex $\boldsymbol{x}_K$ and base σ and by $d_{K,\sigma}\in\mathbb{R}^+$ the orthogonal distance between $\boldsymbol{x}_K$ and σ.

To obtain an HFV discretization of a domain with a fault, we extend this notation to the case of an open set $\Omega\subset\mathbb{R}^N$, for $N=2,3$, which is divided into the subdomains Ω_1 and Ω_2 by an interface (planar if $N=3$,linear if $N=2$) fault $\hat{\gamma}$.

Notation 2 (Discretization of $(\Omega,\hat{\gamma})$) For a domain $\Omega\subset\mathbb{R}^N$ divided into the subdomains Ω_1 and Ω_2 by an interface fault $\hat{\gamma}$, we construct a discretization $(\mathcal{D},\hat{\mathcal{D}})$ from discretizations $\mathcal{D}_j=(\mathcal{M}_j,\mathcal{E}_j,\mathcal{P}_j)$ of Ω_j and from, in the case of the SLRM, a discretization $\hat{\mathcal{D}}=(\hat{\mathcal{M}},\hat{\mathcal{E}},\hat{\mathcal{P}})$ of $\hat{\gamma}$ or in the case of the DLRM, discretizations $\hat{\mathcal{D}}_j=(\hat{\mathcal{M}}_j,\hat{\mathcal{E}}_j,\hat{\mathcal{P}}_j)$ of $\hat{\gamma}_j$, where $\hat{\gamma}_j$ is the part of the boundary of Ω_j lying on the fault $\hat{\gamma}$. Then $\mathcal{D}$ is defined to be

$\mathcal{D}=(\mathcal{M},\mathcal{E},\mathcal{P})$ where
$\mathcal{M}=\mathcal{M}_1\cup\mathcal{M}_2,\ \mathcal{E}=\mathcal{E}_1\cup\mathcal{E}_2,\ \mathcal{P}=\mathcal{P}_1\cup\mathcal{P}_2,$

and $\hat{\mathcal{D}}$ is defined by

in the case of the SLRM
$\hat{\mathcal{D}}=(\hat{\mathcal{M}},\hat{\mathcal{E}},\hat{\mathcal{P}})$ as given
or in the case of the DLRM
$\hat{\mathcal{D}}=(\hat{\mathcal{M}},\hat{\mathcal{E}},\hat{\mathcal{P}})$ where
$\hat{\mathcal{M}}=\hat{\mathcal{M}}_1\cup\hat{\mathcal{M}}_2,\ \hat{\mathcal{E}}=\hat{\mathcal{E}}_1\cup\hat{\mathcal{E}}_2,\ \hat{\mathcal{P}}=\hat{\mathcal{P}}_1\cup\hat{\mathcal{P}}_2,$

Denote by $\mathcal{E}_{j,\text{int}}$, the set of internal faces of $\mathcal{E}_j$, and divide the external faces of $\mathcal{E}_j$ into $\mathcal{E}_{j,\Gamma}$, the set of faces lying on the boundary Γ of Ω, and $\mathcal{E}_{j,\hat{\gamma}}$, the set of those lying on the fault $\hat{\gamma}$.

For the SLRM, we will say that the discretization $(\mathcal{D},\hat{\mathcal{D}})$ is conforming if the set of control volumes $\hat{\mathcal{M}}$ is identical to both the set of faces $\mathcal{E}_{1,\hat{\gamma}}$ and the set of faces $\mathcal{E}_{2,\hat{\gamma}}$, i.e., the discretizations $\mathcal{D}_1$ and $\mathcal{D}_2$ match up along $\hat{\gamma}$, and the discretization on $\hat{\gamma}$ is inherited from each of the discretizations

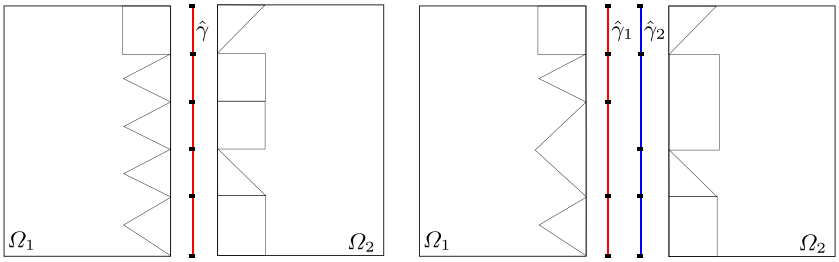

(a) SLRM (b) DLRM

Fig. 3 Example of cells adjacent to the fault for the SLRM and DLRM. These represent conforming meshes in the sense that the fault mesh is inherited from the domain mesh

$\mathcal{D}_1$ and $\mathcal{D}_2$. Then, if $\hat{K} \in \hat{\mathcal{M}}$, a face in $\mathcal{E}_{j,\hat{\gamma}}$ coinciding with $\hat{K}$ will be denoted $\sigma_{\hat{K},j}$.

In the case of the DLRM, the discretization $(\mathcal{D}, \hat{\mathcal{D}})$ is said to be conforming if the set of cells in $\hat{\mathcal{M}}_j$ is identical with the set of faces $\mathcal{E}_{j,\hat{\gamma}}$. However, the two discretizations $\hat{\mathcal{D}}_j$ (when viewed as discretizations on $\hat{\gamma}_j$) are not required to be identical. Then, if $\hat{K}_j \in \hat{\mathcal{M}}_j$, a face in $\mathcal{E}_{j,\hat{\gamma}}$ coinciding with $\hat{K}_j$ will be denoted $\sigma_{\hat{K}_j}$.

See Fig. 3 for an example of meshes. For a discretization $(\mathcal{D}, \hat{\mathcal{D}})$, the pressure in the matrix is approximated by a scalar value p_K in each cell $K \in \mathcal{M}$ and by a scalar value p_σ for each face $\sigma \in \mathcal{E}$. Similarly, the pressure in the fault is approximated by a scalar value $\hat{p}_{\hat{K}}$ in each cell $\hat{K} \in \hat{\mathcal{M}}$ and by a scalar value $\hat{p}_{\hat{\sigma}}$ on each face $\hat{\sigma} \in \hat{\mathcal{E}}$. So the discrete solution which we will denote $(p, \hat{p})$, with apologies for the abuse of notation, associated with $(\mathcal{D}, \hat{\mathcal{D}})$ is of the form

$$p = ((p_K)_{K\in\mathcal{M}}, (p_\sigma)_{\sigma\in\mathcal{E}})$$
$$\hat{p} = \left((\hat{p}_{\hat{K}})_{\hat{K}\in\hat{\mathcal{M}}}, (\hat{p}_{\hat{\sigma}})_{\hat{\sigma}\in\hat{\mathcal{E}}}\right)$$

with p_K, p_σ, $\hat{p}_{\hat{K}}$,and $\hat{p}_{\hat{\sigma}}$ representing an approximation of the average value of p in K, σ, $\hat{K}$, and $\hat{\sigma}$, respectively. Thus for the SLRM with a conforming discretization $(\mathcal{D}, \hat{\mathcal{D}})$, a cell $\hat{K} \in \hat{\mathcal{M}}$ is also both a face $\sigma_1 \in \mathcal{E}_{1,\hat{\gamma}}$ and a face $\sigma_2 \in \mathcal{E}_{2,\hat{\gamma}}$ and will thus be associated with three values $\hat{p}_{\hat{K}}$, p_{σ_1}, and p_{σ_2}. Similarly for the DLRM with a conforming discretization $(\mathcal{D}, \hat{\mathcal{D}})$, if a cell in $\hat{\mathcal{M}}_1$ is also a cell in $\hat{\mathcal{M}}_2$, it will be associated with four values; cf. Fig. 4.

4.1.2 A HFV scheme for the rock matrix

The discrete problem for the HFV scheme is based on the variational form of the continuous problem (11) and requires the definition of a discrete gradient. Once the discrete gradient $\nabla_{\mathcal{D}}$ is defined, the bilinear form Eq. 8 is approximated by replacing the gradient with the discrete gradient in its definition. To define the discrete gradient operator, we begin by defining for each $K \in \mathcal{M}$ a cell gradient:

$$\nabla_K p := \frac{1}{|K|} \sum_{\sigma\in\mathcal{E}_K} |\sigma| (p_\sigma - p_K) \boldsymbol{n}_{K,\sigma}$$

and for each face $\sigma \in \mathcal{E}_K$, a stabilization term for the cone $D_{K,\sigma}$ with vertex x_K and base σ ($D_{K,\sigma} \subset K$):

$$R_{K,\sigma} p := \frac{\beta}{d_{K,\sigma}} [p_\sigma - p_K - \nabla_K p \cdot (\boldsymbol{x}_\sigma - \boldsymbol{x}_K)],$$

where $\beta = \sqrt{\alpha N}$, and $\alpha \in \mathbb{R}^+$ is a stabilization parameter which can vary from cell to cell, see Appendix A.2.2. Then, the discrete gradient for the matrix domain is defined by

$$\nabla_{\mathcal{D}} p|_{D_{K,\sigma}} := \nabla_K p + R_{K,\sigma} p \boldsymbol{n}_{K,\sigma}.$$

The discrete gradient $\nabla_{\mathcal{D}} p$ is thus piecewise constant, constant on each cone $D_{K,\sigma}$, $K \in \mathcal{M}, \sigma \in \mathcal{E}_{K,\sigma}$.

4.1.3 A HFV scheme for the fault

For implementation in the SLRM or DLRM, we also need a discrete (tangential) gradient in the fault which is defined similarly. Once the discrete tangential gradient $\hat{\nabla}_{\mathcal{D}}$

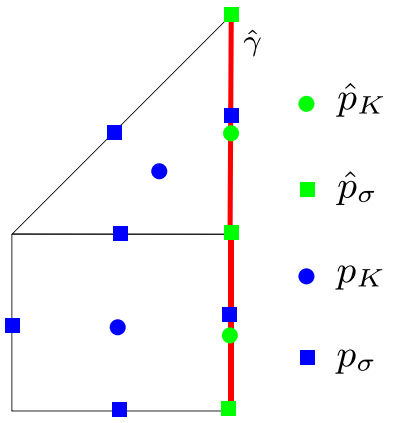

Fig. 4 Example, in the case of the SLRM, of a mesh for $(\Omega, \hat{\gamma})$ with a representation of the *d.o.f.*'s. In the case of the DLRM, the *d.o.f.*'s in the fault are doubled

is defined, the bilinear form Eq. 9 is approximated by replacing the tangential gradient with the discrete tangential gradient in its definition. For each $\hat{K} \in \hat{\mathcal{M}}$, the (fault) cell gradient is defined by

$$\hat{\nabla}_{\hat{K}}\, \hat{p} := \frac{1}{|\hat{K}|} \sum_{\hat{\sigma} \in \mathcal{E}_{\hat{K}}} |\hat{\sigma}| \left(\hat{p}_{\hat{\sigma}} - \hat{p}_{\hat{K}}\right) \boldsymbol{\hat{n}}_{\hat{K},\hat{\sigma}}, \tag{16}$$

and for each $\hat{\sigma} \in \hat{\mathcal{E}}_{\hat{K}}$, the stabilization term $R_{\hat{K},\hat{\sigma}}$ is defined on the cone $D_{\hat{K},\hat{\sigma}}$ by

$$R_{\hat{K},\hat{\sigma}}\, \hat{p} := \frac{\hat{\beta}}{d_{\hat{K},\hat{\sigma}}} \left[\hat{p}_{\hat{\sigma}} - \hat{p}_{\hat{K}} - \hat{\nabla}_{\hat{K}}\, \hat{p} \cdot \left(\boldsymbol{x}_{\hat{\sigma}} - \boldsymbol{x}_{\hat{K}}\right) \right], \tag{17}$$

where $\hat{\beta} = \sqrt{\hat{\alpha}(N-1)}$ and $\hat{\alpha} \in \mathbb{R}^+$ is a stabilization parameter for the fault cell $\hat{K}$. Then, as in the matrix, the discrete (tangential) gradient for the fault domain $\hat{\gamma}$ is defined cone by cone:

$$\hat{\nabla}_{\mathcal{D}}\, \hat{p}\Big|_{D_{\hat{K},\hat{\sigma}}} := \hat{\nabla}_{\hat{K}}\, \hat{p} + R_{\hat{K},\hat{\sigma}}\, \hat{p}\, \boldsymbol{\hat{n}}_{\hat{K},\hat{\sigma}}. \tag{18}$$

4.1.4 Coupling between the rock matrix and the fault

The HFV equations in the matrix domain and those in the fault then must be coupled through a discrete version of the coupling equations. For the SLRM with a conforming discretization $(\mathcal{D}, \hat{\mathcal{D}})$, this approximation is quite simple; the bilinear form $cc((\cdot,\cdot),(\cdot,\cdot))$ of Eq. 14 is approximated as follows: for $(p, \hat{p})$ and $(v, \hat{v})$ in $\mathcal{V} \times \hat{\mathcal{V}}$,

$$\begin{aligned} cc\big((p,\hat{p}),(v,\hat{v})\big) \approx & \sum_{\hat{K} \in \hat{M}} \frac{\hat{\lambda}_{\boldsymbol{n}}}{2} |\hat{K}|\, [\![p]\!]_{\hat{K}}\, [\![v]\!]_{\hat{K}} \\ & + \sum_{\hat{K} \in \hat{M}} 2\hat{\lambda}_{\boldsymbol{n}} |\hat{K}| \left(\{\!\{p\}\!\}_{\hat{K}} - \hat{p}_{\hat{K}}\right) \left(\{\!\{v\}\!\}_{\hat{K}} - \hat{v}_{\hat{K}}\right). \end{aligned} \tag{19}$$

where the jump and the average term are given by

$$[\![p]\!]_{\hat{K}} = p_{\sigma_{\hat{K},1}} - p_{\sigma_{\hat{K},2}}, \quad \{\!\{p\}\!\}_{\hat{K}} = \frac{p_{\sigma_{\hat{K},1}} + p_{\sigma_{\hat{K},2}}}{2},$$

with $\sigma_{\hat{K},j}$ the face in $\mathcal{E}_{j,\hat{\gamma}}$ coinciding with $\hat{K}$.

For the DLRM, even with a conforming discretization, the fault cells in $\hat{\mathcal{M}}_1$ do not match up with those in $\hat{\mathcal{M}}_2$ and this non matching between the two layers must be taken into account. Here, the expression for the bilinear form $cc((\cdot,\cdot),(\cdot,\cdot))$ given in Eq. 10 is used. For the first term of Eq. 10, we must consider a common refinement of the meshes $\hat{\mathcal{M}}_j$. We let $\hat{\hat{\mathcal{M}}}$ be the smallest common refinement

$$\hat{\hat{\mathcal{M}}} = \{\hat{\hat{K}} = \hat{K}_1 \cap \hat{K}_2 \neq \emptyset \,:\, \hat{K}_j \in \hat{\mathcal{M}}_j\},$$

and the approximation is given by

$$\sum_{\hat{\hat{K}} \in \hat{\hat{\mathcal{M}}}} \hat{\lambda}_{\boldsymbol{n}} |\hat{\hat{K}}| (\hat{p}_{\hat{K}_{\hat{\hat{K}},1}} - \hat{p}_{\hat{K}_{\hat{\hat{K}},2}})(\hat{v}_{\hat{K}_{\hat{\hat{K}},1}} - \hat{v}_{\hat{K}_{\hat{\hat{K}},2}}), \tag{20}$$

where $\hat{K}_{\hat{\hat{K}},j} \in \hat{\mathcal{M}}_j$ is such that $\hat{\hat{K}} = \hat{K}_{\hat{\hat{K}},1} \cap \hat{K}_{\hat{\hat{K}},2}$. The second term of Eq. 10, which is not affected by the fact that the discretizations of the two layers of the fault may not coincide, is approximated simply by

$$\sum_j \sum_{\hat{K}_j \in \hat{\mathcal{M}}_j} 2\hat{\lambda}_{\boldsymbol{n}} |\hat{K}_j| (p_{\sigma_{\hat{K}_j}} - \hat{p}_{\hat{K}_j})(v_{\sigma_{\hat{K}_j}} - \hat{v}_{\hat{K}_j}), \tag{21}$$

where $\sigma_{\hat{K}_j}$ is the face in $\mathcal{E}_{\hat{\gamma},j}$ coinciding with $\hat{K}_j$.

4.2 Discretization with virtual fault cells

We consider another type of discretization based on a different construction of the fault mesh. This second approach avoids the explicit construction of the tangential operators placing all of the complexity of the approximation on the construction of the fault mesh. We start with a conforming discretization $(\mathcal{D}, \hat{\mathcal{D}})$ as described in the preceding subsection and construct a new discretization $(\mathcal{D}, \widehat{\mathcal{D}})$ consisting only of N-dimensional cells. This second method of discretization in fact is made by giving width to the interface cells in the direction normal to the interface and can be seen in some loose sense as the inverse of the process used to obtain the reduced model. We will use the wide hat notation $\widehat{\cdot}$ to denote objects pertaining to the virtual fault domain.

Definition 1 (Virtual fault cell - SLRM) Given $\hat{K} \in \hat{\mathcal{M}}$, we construct an N-dimensional cell $\widehat{K}$, called a *virtual fault cell*, by expanding $\hat{K}$ in both directions $\pm\boldsymbol{n}$, normal to the fault:

$$\widehat{K} = \left\{ \boldsymbol{x} = \hat{\boldsymbol{x}} + \frac{\xi d}{2}\boldsymbol{n} \in \mathbb{R}^N : \hat{\boldsymbol{x}} \in \hat{K}, |\xi| < 1 \right\}.$$

Definition 2 (Virtual fault cell - DLRM) Given $\hat{K} \in \hat{\mathcal{M}}_j$, we construct the N-dimensional cell $\widehat{K}$, called a *virtual fault cell*, by expanding $\hat{K}$ in the normal direction but only on one side of the fault, the side toward Ω_j, i.e., in the direction $(-1)^j\boldsymbol{n}$:

$$\widehat{K} = \left\{ \boldsymbol{x} = \hat{\boldsymbol{x}} + (-1)^j \frac{\xi d}{2}\boldsymbol{n} : \hat{\boldsymbol{x}} \in \hat{K}, 0 \leq \xi < 1 \right\}.$$

In Fig. 5, we show an example of the construction of virtual cells for both the SLRM and DLRM.

We consider the mesh $\widehat{\mathcal{M}}$ for the faults defined to be the collection of all the virtual cells. We will also need a set of faces $\widehat{\mathcal{E}}$ and a set of points $\widehat{\mathcal{P}}$.

Definition 3 (Discretization of $\hat{\gamma}$ by virtual cells - SLRM) Given a conforming discretization $(\mathcal{D}, \hat{\mathcal{D}})$ of $(\Omega, \hat{\gamma})$ as defined in Notation 2, the corresponding discretization of $\hat{\gamma}$ by virtual fault cells is defined to be the triplet $\widehat{\mathcal{D}} := \left(\widehat{\mathcal{M}}, \widehat{\mathcal{E}}, \widehat{\mathcal{P}}\right)$, where $\widehat{\mathcal{M}}$ is the set of virtual fault cells obtained

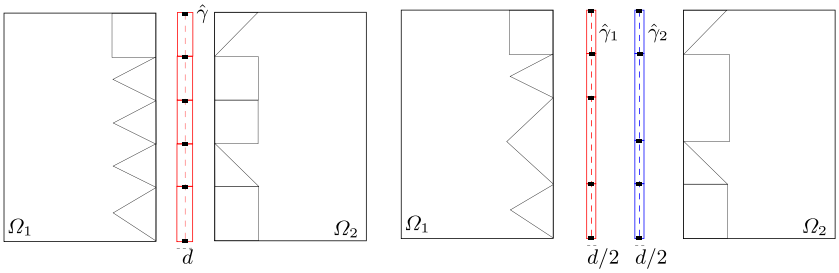

(a) SLRM (b) DLRM

Fig. 5 Representation of virtual cells, in *red* and *blue*, for a general configuration

by expanding the cells of $\hat{\mathcal{M}}$, $\widehat{\mathcal{E}}$ is the set of $((N-1)$-dimensional) faces of cells in $\widehat{\mathcal{M}}$, and $\widehat{\mathcal{P}}$ is the set of points that are the barycentres of elements of $\widehat{\mathcal{M}}$ or of elements of $\widehat{\mathcal{E}}$.

Now, we construct the set $\mathcal{M}' = \mathcal{M} \cup \widehat{\mathcal{M}}$ but in which we identify the faces in $\mathcal{E}_{j,\hat{\gamma}}$ with the corresponding faces in $\widehat{\mathcal{E}}$ on the jth side of $\hat{\gamma}$. In this manner, we obtain a set of cells $\mathcal{M}'$ which may be thought of as a mesh for the "virtual domain" $\widehat{\Omega}$ obtained from Ω by expanding the "flat domain" $\hat{\gamma}$ to obtain an N-dimensional fault domain of width d. More precisely, since we have assumed that the discretization $(\mathcal{D}, \hat{\mathcal{D}})$ is conforming, each face $\sigma_j \in \mathcal{E}_{j,\hat{\gamma}}$ coincides with a cell $\hat{K} \in \hat{\mathcal{M}}$, that we may denote $\hat{K}_{\sigma_j}$. Then the virtual cell $\widehat{K}_{\sigma_j} \in \widehat{\mathcal{M}}$ obtained by expanding $\hat{K}_{\sigma_j}$ has one face $\sigma_{\widehat{K}_{\sigma_j}}$ parallel to $\hat{K}_{\sigma_j}$ and on the jth side of $\hat{K}_{\sigma_j}$, and we shall identify this face with σ_j. There will be only one pressure unknown associated with each face σ_j, i.e., $p_{\sigma_j} = p_{\sigma_{\widehat{K}_{\sigma_j}}}$. Then with $\mathcal{E}'$ and $\mathcal{P}'$ defined in the obvious manner, we may consider the discretization $\mathcal{D}' = (\mathcal{M}', \mathcal{E}', \mathcal{P}')$ as a discretization of the domain

$$\overline{\widehat{\Omega}} := \overline{\Omega_1} \cup \overline{\Omega_2} \cup \overline{\widehat{\gamma}},$$

where $\widehat{\gamma}$ is the interior of the union of the closures of the virtual cells in $\widehat{\mathcal{M}}$. Now, we may apply the standard HFV method to the discretization $\mathcal{D}'$ of $\widehat{\Omega}$.

We will show below that, under certain hypotheses, this scheme is equivalent to the scheme defined earlier.

Remark 2 In the general case where the fault segments are not collinear, it is still possible to build up the virtual cells; however, a more careful description of the pairs of degrees of freedom should be considered. Moreover, the virtual cells may overlap each others. In Section 5, we consider faults made of non collinear elements. See Fig. 6 for an example of virtual cells for a general mesh.

4.3 Comparison of the two approaches

In this subsection, we prove two results that can be useful for the implementation of the proposed method. In particular, we show that for the SLRM, the implementation of the HFV method for the reduced model by the method with virtual cells as described in Section 4.2 is equivalent to the implementation with the discretization described in Section 4.1 cf. also [34, section 5] where a similar result for the SLRM discretized with a mixed method was used to establish error estimates. For the DLRM, we show equivalence of modifications of the two methods obtained by discretizing in the fault with a two-point flux scheme instead of the HFV method while retaining the HFV method for discretization in the matrix cells of $\mathcal{M}_1$ and $\mathcal{M}_2$ and retaining the discretization given for the coupling conditions.

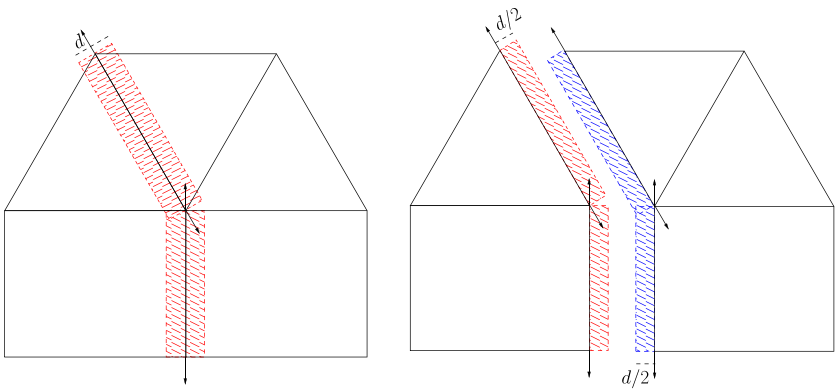

(a) SLRM (b) DLRM

Fig. 6 Example of construction of virtual cells, for both the SLRM and DLRM, for a general configuration. The *arrow* in the figure are the outward normals for the tangential part of the fault cells

4.3.1 Discrete equivalence of SLRM

In this part, we detail the equivalence, at discrete level for the SLRM, of the HFV numerical scheme applied directly to the reduced model and the virtual cell approach.

Theorem 1 (Discrete equivalence - SLRM) *For a domain Ω with an interface fault $\hat{\gamma}$ modeled with the SLRM and a conforming discretization $(\mathcal{D}, \hat{\mathcal{D}})$, the numerical solution obtained using the HFV method of Section 4.1 with stabilization parameters α and $\hat{\alpha}$ satisfying $\alpha N = 2$ and $\alpha N = 2\hat{\alpha}(N-1)$ is equivalent to that obtained using the HFV method with stabilization parameter α for the associated virtual fault discretization $\mathcal{D}' = (\mathcal{D}, \widehat{\mathcal{D}})$ of the virtual domain $\widehat{\Omega}$ described in Section 4.2.*

Proof For simplicity, we give the proof only in the case in which $N = 2$, the proof in the case $N = 3$ being quite similar. Also for simplicity, we assume that Λ_f is constant. It is easy to check that there is an obvious correspondence between the unknown values

$$p = ((p_K)_{K\in\mathcal{M}}, (p_\sigma)_{\sigma\in\mathcal{E}}) \text{ and}$$
$$\hat{p} = \left((\hat{p}_{\hat{K}})_{\hat{K}\in\hat{\mathcal{M}}}, (\hat{p}_{\hat{\sigma}})_{\hat{\sigma}\in\hat{\mathcal{E}}}\right)$$

for the standard HFV discretization for the reduced model and those for the discretization with virtual fault cells

$$p' = \left((p'_K)_{K\in\mathcal{M}'}, (p'_\sigma)_{\sigma\in\mathcal{E}'}\right);$$

see Fig. 7.

For the SLRM, the bilinear form $a\big((\cdot,\cdot),(\cdot,\cdot)\big) + cc\big((\cdot,\cdot),(\cdot,\cdot)\big)$ of Eq. 11 is made up of four parts: $a_\Omega(\cdot,\cdot), a_{\hat{\gamma}}(\cdot,\cdot)$ and the two terms of $cc\big((\cdot,\cdot),(\cdot,\cdot)\big)$ as given in Eq. 14. For the virtual fault scheme the weak formulation takes the form

$$\begin{aligned} &\text{find } p \in \mathcal{V}_{\widehat{\Omega}} \text{ such that} \\ &a_{\widehat{\Omega}}(p, v) = F(v), \\ &\text{for all } v \in \mathcal{V}_{\widehat{\Omega}}, \end{aligned} \tag{22}$$

where $\mathcal{V}_{\widehat{\Omega}} = H^1_\Gamma(\widehat{\Omega})$ and where

$$a_{\widehat{\Omega}}(p, v) := (\Lambda\nabla p, \nabla v)_{\widehat{\Omega}}\,.$$

To compare the two schemes, we first observe that for p and v in $\mathcal{V}_{\widehat{\Omega}}$,we have

$$a_{\widehat{\Omega}}(p, v) = (\Lambda\nabla p, \nabla v)_{\Omega_1\cup\Omega_2} + (\Lambda\nabla p, \nabla v)_{\widehat{\gamma}}\,, \tag{23}$$

where $\widehat{\gamma}$ is the interior of the union of the closures of the virtual cells. Then, we compare the approximations of these bilinear forms. As the terms from the form $a_\Omega(\cdot,\cdot)$ are exactly the same as those in the first term in the decomposition of $a_{\widehat{\Omega}}(\cdot,\cdot)$ given in Eq. 23, and they are approximated in precisely the same manner, we are left to compare the approximation of $a_{\hat{\gamma}}(\cdot,\cdot) + cc((\cdot,\cdot),(\cdot,\cdot))$ with that of the second term of the decomposition of $a_{\widehat{\Omega}}(\cdot,\cdot)$ given in Eq. 23.

From Eq. 19, we see that the bilinear form $cc\big((\cdot,\cdot),(\cdot,\cdot)\big)$ of Eq. 14 is approximated as follows: for $(p,\hat{p})$ and $(v,\hat{v})$ in $\mathcal{V}\times\hat{\mathcal{V}}$,

$$\begin{aligned} cc\big((p,\hat{p}),(v,\hat{v})\big) \approx &\sum_{\hat{K}\in\hat{\mathcal{M}}} \frac{\hat{\lambda}_{\boldsymbol{n}}}{2}\big|\hat{K}\big|\,[\![p]\!]_{\hat{K}}\,[\![v]\!]_{\hat{K}} \\ &+ \sum_{\hat{K}\in\hat{\mathcal{M}}} 2\hat{\lambda}_{\boldsymbol{n}}\big|\hat{K}\big|\left(\{\!\{p\}\!\}_{\hat{K}} - \hat{p}_{\hat{K}}\right)\left(\{\!\{p\}\!\}_{\hat{K}} - \hat{v}_{\hat{K}}\right). \end{aligned} \tag{24}$$

From Eqs. 16–18, we calculate that the bilinear form $a_{\hat{\gamma}}(\cdot,\cdot)$ of Eq. 13, corresponding to the tangential flow Eq. 12b, is approximated as follows: for $\hat{p}$ and $\hat{v}$ in $\hat{\mathcal{V}}$,

$$\begin{aligned} a_{\hat{\gamma}}(\hat{p},\hat{v}) &= \sum_{\hat{K}\in\hat{\mathcal{M}}}\int_{\hat{K}} 2\hat{\lambda}\nabla_{\boldsymbol{\tau}}\hat{p}\cdot\nabla_{\boldsymbol{\tau}}\hat{v}\,\mathrm{d}\hat{x} \\ &\approx \sum_{\hat{K}\in\hat{\mathcal{M}}}\int_{\hat{K}} 2\hat{\lambda}\hat{\nabla}_{\mathcal{D}}\,\hat{p}\cdot\hat{\nabla}_{\mathcal{D}}\,\hat{v}\,\mathrm{d}\hat{x} \\ &= \sum_{\hat{K}\in\hat{\mathcal{M}}} 2\hat{\lambda}\big|\hat{K}\big|\hat{\nabla}_{\hat{K}}\hat{p}\cdot\hat{\nabla}_{\hat{K}}\hat{v} \\ &\quad + 2\sum_{\hat{K}\in\hat{\mathcal{M}}}\hat{\lambda}\big|\hat{K}\big|\sum_{j=1}^{2} R_{\hat{K},\hat{\sigma}_{\hat{K},j}}\hat{p}\,R_{\hat{K},\hat{\sigma}_{\hat{K},j}}\hat{v}, \end{aligned}$$

where $\hat{\sigma}_{\hat{K},1}$ and $\hat{\sigma}_{\hat{K},2}$ are the two faces (i.e., vertices) of $\hat{K}$, which we suppose are numbered such that the vector pointing from $\hat{\sigma}_{\hat{K},2}$ toward $\hat{\sigma}_{\hat{K},1}$ is oriented in the same direction as $\boldsymbol{\tau}$, so that the second summation in the last term is over the two cones (i.e., half segments) of $\hat{K}$. The cell gradient may be written

$$\hat{\nabla}_{\hat{K}}\hat{p} = \frac{1}{\big|\hat{K}\big|}\delta_{\hat{K}}(\hat{p}_{\hat{\sigma}})\boldsymbol{\tau},$$

where we have written $\delta_{\hat{K}}(\hat{p}_{\hat{\sigma}})$ for $\hat{p}_{\hat{\sigma}_{\hat{K},1}} - \hat{p}_{\hat{\sigma}_{\hat{K},2}}$, while the stabilization term in the cone $D_{\hat{K},\hat{\sigma}_{\hat{K},j}}$ is

$$R_{\hat{K},\hat{\sigma}_{\hat{K},j}}\hat{p} = (-1)^j\frac{\hat{\beta}}{\big|\hat{K}\big|/2}\left(\mu_{\hat{K}}(\hat{p}_{\hat{\sigma}}) - \hat{p}_{\hat{K}}\right),$$

where we have denoted by $\mu_{\hat{K}}(\hat{p}_{\hat{\sigma}})$ the average value $(\hat{p}_{\hat{\sigma}_{\hat{K},1}} + \hat{p}_{\hat{\sigma}_{\hat{K},2}})/2$. So we may now write the approximation for the bilinear form $a_{\hat{\gamma}}(\cdot,\cdot)$,as follows:

$$\begin{aligned} a_{\hat{\gamma}}(\hat{p},\hat{v}) \approx &\sum_{\hat{K}\in\hat{\mathcal{M}}}\frac{2\hat{\lambda}}{\big|\hat{K}\big|}\delta_{\hat{K}}(\hat{p}_{\hat{\sigma}})\delta_{\hat{K}}(\hat{v}_{\hat{\sigma}}) \\ &+ \sum_{\hat{K}\in\hat{\mathcal{M}}}\frac{8\hat{\lambda}\hat{\beta}^2}{\big|\hat{K}\big|}\left(\mu_{\hat{K}}(\hat{p}_{\hat{\sigma}}) - \hat{p}_{\hat{K}}\right)\left(\mu_{\hat{K}}(\hat{v}_{\hat{\sigma}}) - \hat{v}_{\hat{K}}\right), \end{aligned} \tag{25}$$

with $\hat{\beta} = \sqrt{\hat{\alpha}(N-1)}$.

We next need to make explicit the terms in the approximation of the second term in the decomposition given in

Eq. 23 of $a_{\widehat{\Omega}}(\cdot,\cdot)$ which we then split into tangential and normal components: for p and v in $\mathcal{V}_{\widehat{\Omega}}$,

$$\begin{aligned}(\Lambda\nabla p,\nabla v)_{\widehat{\gamma}} &\approx \sum_{\widehat{K}\in\widehat{\mathcal{M}}}\int_{\widehat{K}}\nabla_{\mathcal{D}}\, p\cdot\Lambda\nabla_{\mathcal{D}}\, v\mathrm{d}\boldsymbol{x}\\ &= \sum_{\widehat{K}\in\widehat{\mathcal{M}}}\int_{\widehat{K}} N\nabla_{\mathcal{D}}\, p\cdot\Lambda N\nabla_{\mathcal{D}}\, v\mathrm{d}\boldsymbol{x}\\ &+ \sum_{\widehat{K}\in\widehat{\mathcal{M}}}\int_{\widehat{K}} \boldsymbol{T}\nabla_{\mathcal{D}}\, p\cdot\Lambda\boldsymbol{T}\nabla_{\mathcal{D}}\, v\mathrm{d}\boldsymbol{x}.\end{aligned}$$

For $\widehat{K}\in\widehat{\mathcal{M}}$ and $\sigma_{\widehat{K},j}$, the face of $\widehat{K}$ identified with a face in $\mathcal{E}_{j,\hat{\gamma}}$ and $\widehat{\sigma}_{\widehat{K},1}$ and $\widehat{\sigma}_{\widehat{K},2}$ the remaining two faces of $\widehat{K}$ numbered such that $\boldsymbol{\tau}$ points from the midpoint of $\widehat{\sigma}_{\widehat{K},2}$ toward that of $\widehat{\sigma}_{\widehat{K},1}$, (see Fig. 7) the cell gradient maybe written as follows:

$$\nabla_{\widehat{K}}p=-\frac{1}{d}(p_{\sigma_{\widehat{K},1}}-p_{\sigma_{\widehat{K},2}})\boldsymbol{n}+\frac{1}{|\widehat{K}|}(p_{\widehat{\sigma}_{\widehat{K},1}}-p_{\widehat{\sigma}_{\widehat{K},2}})\boldsymbol{\tau},$$

where we recall that $\widehat{K}$ is a rectangle with $|\widehat{K}|=d|\hat{K}|$, while the four stabilization terms are

$$\begin{aligned}R_{\widehat{K},\sigma_{\widehat{K},j}}p\boldsymbol{n}_{\widehat{K},\sigma_{\widehat{K},j}}&=(-1)^j\frac{2\beta}{d}\big(\mu_{\widehat{K}}(p_\sigma)-p_{\widehat{K}}\big)\boldsymbol{n}\\ R_{\widehat{K},\widehat{\sigma}_{\widehat{K},j}}p\boldsymbol{n}_{\widehat{K},\widehat{\sigma}_{\widehat{K},j}}&=(-1)^{j+1}\frac{2\beta}{|\widehat{K}|}\big(\mu_{\widehat{K}}(p_{\widehat{\sigma}})-p_{\widehat{K}}\big)\boldsymbol{\tau},\end{aligned}$$

with the average terms $\mu_{\widehat{K}}(p_\sigma)=(p_{\sigma_{\widehat{K},1}}+p_{\sigma_{\widehat{K},2}})/2$ and $\mu_{\widehat{K}}(p_{\widehat{\sigma}})=(p_{\widehat{\sigma}_{\widehat{K},1}}+p_{\widehat{\sigma}_{\widehat{K},2}})/2$. The contribution from the normal part of the discrete term is thus

$$\begin{aligned}&\sum_{\widehat{K}\in\widehat{\mathcal{M}}}\int_{\widehat{K}}\boldsymbol{N}\nabla_{\mathcal{D}}\, p\cdot\Lambda\boldsymbol{N}\nabla_{\mathcal{D}}\, v\mathrm{d}\boldsymbol{x}\\ &=\sum_{\widehat{K}\in\widehat{\mathcal{M}}}\frac{\hat{\lambda}_{\boldsymbol{n}}}{2}|\hat{K}|\delta_{\widehat{K}}(p_\sigma)\delta_{\widehat{K}}(v_\sigma)\\ &+\sum_{\widehat{K}\in\widehat{\mathcal{M}}}\hat{\lambda}_{\boldsymbol{n}}|\hat{K}|\beta^2\big(\mu_{\widehat{K}}(p_\sigma)-p_{\widehat{K}}\big)\big(\mu_{\widehat{K}}(v_\sigma)-v_{\widehat{K}}\big),\end{aligned}\tag{26}$$

while that from the tangential part is

$$\begin{aligned}&\sum_{\widehat{K}\in\widehat{\mathcal{M}}}\int_{\widehat{K}}\boldsymbol{T}\nabla_{\mathcal{D}}\, p\cdot\Lambda\boldsymbol{T}\nabla_{\mathcal{D}}\, v\mathrm{d}\boldsymbol{x}\\ &=\sum_{\widehat{K}\in\widehat{\mathcal{M}}}\frac{2\hat{\lambda}}{|\widehat{K}|}\delta_{\widehat{K}}(p_{\widehat{\sigma}})\delta_{\widehat{K}}(v_{\widehat{\sigma}})\\ &+\sum_{\widehat{K}\in\widehat{\mathcal{M}}}\frac{4\hat{\lambda}\beta^2}{|\widehat{K}|}\big(\mu_{\widehat{K}}(p_{\widehat{\sigma}})-p_{\widehat{K}}\big)\big(\mu_{\widehat{K}}(v_{\widehat{\sigma}})-v_{\widehat{K}}\big),\end{aligned}\tag{27}$$

with $\delta_{\widehat{K}}(p_\sigma)=p_{\sigma_{\widehat{K},1}}-p_{\sigma_{\widehat{K},2}}$ and $\delta_{\widehat{K}}(p_{\widehat{\sigma}})=p_{\widehat{\sigma}_{\widehat{K},1}}-p_{\widehat{\sigma}_{\widehat{K},2}}$, and $\beta=\sqrt{\alpha N}$. Now identifying for each $\hat{K}\in\hat{\mathcal{M}}$, the unknowns $\hat{p}_{\hat{K}}$, $\hat{p}_{\hat{\sigma}_{\hat{K},1}}$, $\hat{p}_{\hat{\sigma}_{\hat{K},2}}$, $p_{\sigma_{\hat{K},1}}$, and $p_{\sigma_{\hat{K},2}}$, respectively, of the HFV discretization of the SLRM with the unknowns $p_{\widehat{K}}$, $p_{\widehat{\sigma}_{\widehat{K},1}}$, $p_{\widehat{\sigma}_{\widehat{K},2}}$, $p_{\sigma_{\widehat{K},1}}$ and $p_{\sigma_{\widehat{K},2}}$, respectively, of the HFV discretization of $\widehat{\Omega}$ using virtual elements, we have that Eq. 26 is equivalent to Eq. 24 if $\beta^2=2$, while Eq. 27 is equivalent to Eq. 25 provided that $2\hat{\beta}^2=\beta^2$. □

4.3.2 Discrete equivalence of DLRM

We turn our attention now to a comparison of the two discretization techniques for the DLRM for a domain Ω with interface fault $\hat{\gamma}=\hat{\gamma}_1=\hat{\gamma}_2$. We suppose that we have a conforming discretization $(\mathcal{D},\hat{\mathcal{D}})$, and recall that this does not imply that $\hat{\mathcal{M}}_1$ coincides with $\hat{\mathcal{M}}_2$. We point out though that in the case that $\hat{\mathcal{M}}_1$ and $\hat{\mathcal{M}}_2$ do coincide the demonstration of Theorem 1 extends immediately to show that the discretization with virtual (N-dimensional) fault cells and that with interface (($N-1$)-dimensional) cells for the fault are equivalent with the appropriate conditions on β and $\hat{\beta}$. However in the general case (when the grids $\hat{\mathcal{M}}_1$ and $\hat{\mathcal{M}}_2$ in the fault are non matching), such an equivalence no longer holds as tangential terms of the discrete gradient are involved in the approximation of the coupling conditions. In the following theorem, however, we do obtain an equivalence when the classical two-point flux approximation (TPFA) scheme is used for the problem inside the fault (while retaining the HFV method in the matrix domains).

Before stating the equivalence theorem for the DLRM, we give a more precise description of the modification of each scheme that is used in the theorem. For the discretization using $(N-1)$-dimensional cells in the fault, the modifications are as follows:

- For the discretization of the bilinear form $a_\Omega(\cdot,\cdot)$, there is no change as the HFV method is still used.
- For the discretization of $a_{\hat{\gamma}}(\cdot,\cdot)$, the HFV method is replaced by the two point flux method: there are no pressure unknowns on the faces $\hat{\sigma}_{\hat{K},j}$ of the cells $\hat{K}\in\hat{\mathcal{M}}$.
- For the discretization of $cc\big((\cdot,\cdot),(\cdot,\cdot)\big)$, there is no change.

For the discretization using virtual (N-dimensional) cells in the fault, we have

- For the discretization of the first term in the decomposition Eq 23 of $a_{\widehat{\Omega}}(\cdot,\cdot)$, there is no change: the HFV method is used.
- For the discretization of the second term in the decomposition (23) of $a_{\widehat{\Omega}}(\cdot,\cdot)$, the two point flux method is used with a minor modification:
  - For the tangential component, the standard two-point flux method is used. There are no pressure unknowns associated with the faces $\widehat{\sigma}_{\widehat{K},j}$ of $\widehat{K}_j\in\widehat{\mathcal{M}}_j$ that lie in the interior of $\widehat{\gamma}$.
  - For the normal component, for a cell $\widehat{K}_j\in\widehat{\mathcal{M}}_j$, as the HFV method has been used in the neighboring

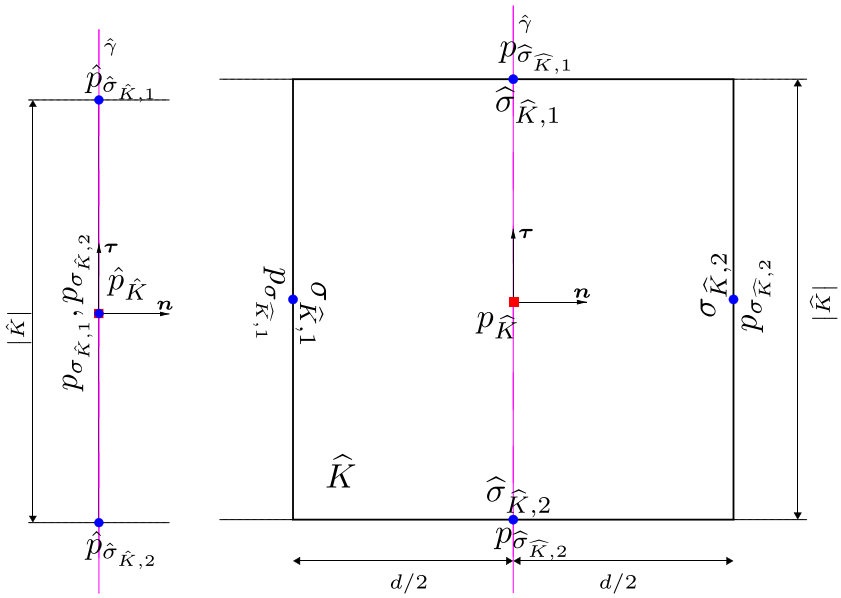

(a) $1D$ (b) $2D$

Fig. 7 Notations for a 1D-cell and a virtual 2D-cell. The names of the unknowns are chosen to easily compare the results

cell $K_j \in \mathcal{M}_j$, there is a pressure value available on the the face $\sigma_{\widehat{K}_j}$ common to the virtual cell $\widehat{K}_j$ and to the cell K_j. The value $p_{\sigma_{\widehat{K}_j}}$ together with the value $p_{\widehat{K}_j}$ is used to approximate the normal component of the gradient of p in $\widehat{K}_j$ (instead of the value p_{K_j}).

The following result shows the equivalence when a two-point flux scheme is considered to approximate the tangential component of the second term of Eq. 23, but would also be the case if we were using the HFV method, provided or course that $2\hat{\beta}^2 = \beta^2$. The proof is given in the simple case of planar faults.

Theorem 2 (Two-points discrete equivalence—DLRM) *Suppose Ω is a domain with an interface fault $\hat{\gamma}$ modeled with the DLRM and that $(\mathcal{D}, \hat{\mathcal{D}})$ is a conforming discretization of $(\Omega, \hat{\gamma})$. The numerical solution obtained using the HFV method of Section 4.1 but a two-point scheme as described above for the fault is equivalent to that obtained using the HFV method for the associated virtual fault discretization $\mathcal{D}' = (\mathcal{D}, \widehat{\mathcal{D}})$ of the virtual domain $\widehat{\Omega}$ described in Section 4.2 with the modification for the virtual cells described above.*

Proof Again for simplicity, we assume $N = 2$ and that Λ_f is constant. As in the proof of Theorem 1, it is sufficient to compare the terms coming from the bilinear forms $cc\big((\cdot,\cdot),(\cdot,\cdot)\big)$ and $a_{\hat{\gamma}}(\cdot,\cdot)$, i.e., from the coupling terms and those associated with flow in the fault, with the terms associated with the second term in Eq. 23. It is also clear that the terms in the discretization of $a_{\hat{\gamma}}(\cdot,\cdot)$ correspond precisely to those in the tangential component of the discretization of the second term of Eq. 23.

So we have left to compare the terms associated with the discretization of $cc\big((\cdot,\cdot),(\cdot,\cdot)\big)$ with those associated with the normal component of the discretization of the second term of Eq. 23. From Eq. 10 and the approximations given in Eqs. 20 and 21, we have the approximation of $cc\big((p,\hat{p}),(v,\hat{v})\big)$ is given as follows:

$$\sum_j \sum_{\hat{K}_j \in \hat{\mathcal{M}}_j} 2\hat{\lambda}_{\boldsymbol{n}} |\hat{K}_j| (p_{\sigma_{\hat{K}_j}} - \hat{p}_{\hat{K}_j})(v_{\sigma_{\hat{K}_j}} - \hat{v}_{\hat{K}_j}) \tag{28}$$

$$+ \sum_{\hat{\hat{K}} \in \hat{\hat{\mathcal{M}}}} \hat{\lambda}_{\boldsymbol{n}} |\hat{\hat{K}}| (\hat{p}_{\hat{K}_{\hat{\hat{K}},1}} - \hat{p}_{\hat{K}_{\hat{\hat{K}},2}})(\hat{v}_{\hat{K}_{\hat{\hat{K}},1}} - \hat{v}_{\hat{K}_{\hat{\hat{K}},2}}), \tag{29}$$

where as in Eq. 20, $\hat{\hat{\mathcal{M}}}$ is the smallest common refinement of $\hat{\mathcal{M}}_1$ and $\hat{\mathcal{M}}_2$, and for $\hat{\hat{K}} \in \hat{\hat{\mathcal{M}}}$, $\hat{K}_{\hat{\hat{K}},j} \in \hat{\mathcal{M}}_j$ is such that $\hat{K}_{\hat{\hat{K}},1} \cap \hat{K}_{\hat{\hat{K}},2} = \hat{\hat{K}}$.

The normal component of the second term of Eq. 23 is $(\lambda_{f,\boldsymbol{n}} \dfrac{\partial p}{\partial \boldsymbol{n}}, \dfrac{\partial v}{\partial \boldsymbol{n}})_{\hat{\gamma}}$ and is approximated by

$$\sum_j \sum_{\widehat{K}_j \in \widehat{\mathcal{M}}_j} 2\hat{\lambda}_{\boldsymbol{n}} |\hat{K}_j| (p_{\sigma_{\widehat{K}_j}} - p_{\widehat{K}_j})(v_{\sigma_{\widehat{K}_j}} - v_{\widehat{K}_j}) \tag{30}$$

$$+ \sum_{\widehat{\hat{K}} \in \widehat{\hat{\mathcal{M}}}} \hat{\lambda}_{\boldsymbol{n}} |\hat{\hat{K}}| (p_{\widehat{K}_{\hat{\hat{K}},2}} - p_{\widehat{K}_{\hat{\hat{K}},1}})(v_{\widehat{K}_{\hat{\hat{K}},2}} - v_{\widehat{K}_{\hat{\hat{K}},1}}), \tag{31}$$

where we have used the fact that for $\widehat{K}_j \in \widehat{\mathcal{M}}_j$,

$$\lambda_{f,\boldsymbol{n}} |\widehat{K}_j| = \lambda_{f,\boldsymbol{n}} \frac{d|\hat{K}_j|}{4} = 2\hat{\lambda}_{\boldsymbol{n}} \left(\frac{d}{4}\right)^2 |\hat{K}_j|,$$

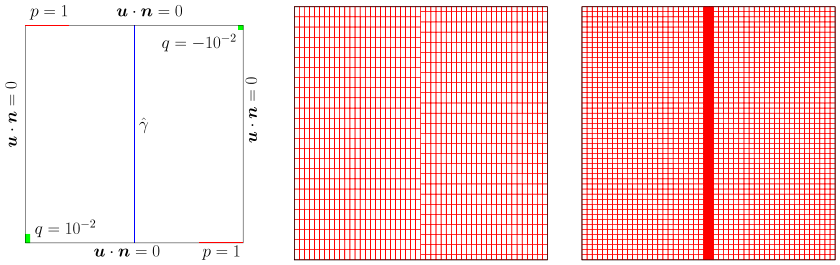

(a) Computational domain. (b) Coarse mesh. (c) Fine mesh.

Fig. 8 Homogeneous academic case: **a** computational domain with some of the data for the problem and meshes. The coarse mesh **b** for the reduced model has 1275 hexahedra outside the fault and 51 elements in the fault, while the fine mesh **c** corresponding to a fine 2-D discretization of the fault has 34,000 hexahedra

and similarly that if $\widehat{\widehat{K}} \in \widehat{\widehat{\mathcal{M}}}$, then

$$\lambda_{f,\boldsymbol{n}} |\widehat{\widehat{K}}| = \lambda_{f,\boldsymbol{n}} \frac{d|\hat{\hat{K}}|}{2} = \hat{\lambda}_{\boldsymbol{n}} \left(\frac{d}{2}\right)^2 |\hat{\hat{K}}|.$$

Now identifying for each $\hat{K}_j \in \hat{\mathcal{M}}_j$, the unknowns $\hat{p}_{\hat{K}_j}$ and $p_{\sigma_{\hat{K}_j}}$, respectively, of the discretization of the DLRM using $(N-1)$-dimensional cells in the fault with the unknowns $p_{\widehat{K}_j}$ and $p_{\sigma_{\widehat{K}_j}}$, respectively, of the discretization of the DLRM using virtual elements in the fault, we have that expression (30) is equivalent to Eq. 28 while expression (31) is equivalent to Eq. 29. □

Remark 3 Theorem 2 shows that the straightforward discretization of the DLRM is similar to a two-point flux approximation of the normal fluxes in the virtual fault cell approach. While this is satisfactory for the fluxes between the fault and its adjacent domain, it is not accurate enough for the fluxes between the two sides of the fault where the grids do not match. Therefore, in the following, we shall only consider the virtual cell approach for which an accurate approximation of the non matching terms is obtained with the HFV scheme.

5 Numerical experiments

In the three following subsections, we present several numerical experiments to validate and assess the proposed double-layer reduced model discretized by the hybrid finite volume scheme. The first subsection is devoted to academic tests for a homogeneous porous medium divided into two subdomains by a single fault while the second section considers instead a layered heterogeneous medium outside the fault. For these two academic tests, we use a direct method to solve the linear systems. The third section is devoted to a realistic test. In all experiments, the coercivity of the discrete bilinear forms is ensured for $\alpha = 1$. Moreover, when $\alpha = 1$, for Cartesian grid the HFV scheme reduces to TPFA. See [26] for a discussion of different values of α.

5.1 Model validity: homogeneous case

We consider the domain $\Omega = (0, 100)^2$, with a vertical fault of thickness $d = 2$ running along the middle of Ω: $\hat{\gamma} = \{(x, y) \in \mathbb{R}^2 : x = 50\}$. See Fig. 8a. We assume Dirichlet boundary conditions for

$$\Gamma_{D,1} = \left\{(x, y) \in \mathbb{R}^2 : y = 100 \text{ and } x < 20\right\}$$
$$\Gamma_{D,2} = \left\{(x, y) \in \mathbb{R}^2 : y = 0 \text{ and } x > 80\right\}$$

with data $p = 1$ and homogeneous Neumann boundary conditions for the rest of the boundary. For the fault, we impose homogeneous Neumann boundary conditions. We set a source term in the regions

$$\Omega_{q,1} = \{(x, y) \in (0, 2) \times (0, 4)\}$$
$$\Omega_{q,2} = \left\{(x, y) \in (98, 100)^2\right\}$$

equal to 10^{-2}, for $\Omega_{q,1}$ and -10^{-2} for $\Omega_{q,2}$.

We consider a coarse mesh where the reduced model is used and a fine mesh corresponding to a fine 2-D discretization of a region including the fault is used. In the

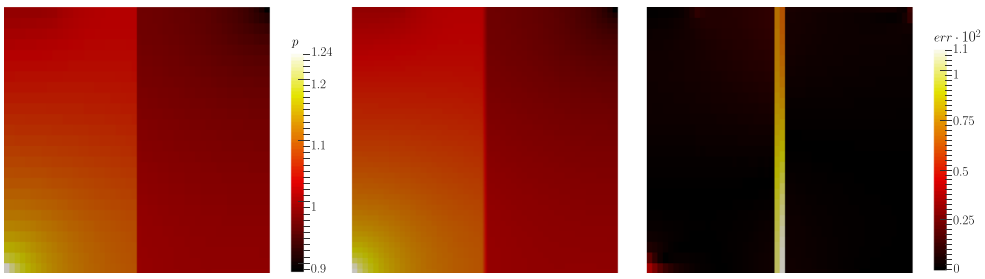

(a) With the *RM*. (b) Without the *RM*. (c) Model error.

Fig. 9 Barrier case: Model error between the reduced model solution on the coarse mesh (Fig. 8b) and the full 2-D model solution on the fine mesh (Fig. 8c)

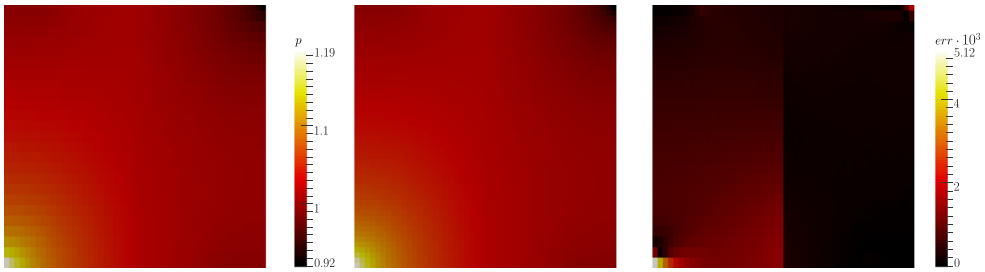

(a) With the *RM*. (b) Without the *RM*. (c) Model error.

Fig. 10 Channel case: Model error between the reduced model solution on the coarse mesh (Fig. 8b) and the full 2-D model solution on the fine mesh (Fig. 8c)

latter method, the fault is discretized with six elements in the normal direction to the fault. See Figs. 8b, c. One should note that for the reduced model, the subdomain meshes do not match (Fig. 8). We introduce the relative error between the solution p_{coarse} obtained with the reduced model and a coarse grid and the full 2-D model solution p_{fine}, that obtained with a fine 2-D discretization of the fault, as an indicator of the validity of the reduced model. For a given cell $K \in \mathcal{M}$, we have

$$err(K) := \frac{\|\Pi p_{\text{fine}} - p_{\text{coarse}}\|_{L^2(K)}}{\|\Pi p_{\text{fine}}\|_{L^2(K)}}, \tag{32}$$

with $\mathcal{M}$ the coarse mesh and Πp_{fine} the interpolation of p_{fine} on the coarse mesh $\mathcal{M}$, setting up the problem such that the pressure field is not zero. Of course, this definition of the error gives a larger error than one would obtain with an error calculated by comparing the pressure in the matrix obtained with the reduced model with that obtained using the non-reduced model and then comparing the corresponding pressures in the fracture. With the error as we define it here, on a very narrow strip surrounding the fracture, we are actually comparing a pressure in the fracture (from the non-reduced model) with a pressure in the matrix (from the reduced model).

We consider three test cases corresponding to different permeabilities in the fault while maintaining the identity matrix for the permeability tensor in Ω_i for $i = 1, 2$.

We choose as the permeability in the fault $\Lambda_f = \text{diag}\left\{10^{-2}, 1\right\}$. In Fig. 9, we show the solutions obtained with the reduced model, Fig. 9a, with the full 2-D model on a refined mesh, Fig. 9b, and the error between them $err(K)$ given by Eq. 32, (Fig. 9c). We observe that the largest part of the error is concentrated in the strip along the fracture where fracture pressure is being compared with matrix pressure. This is as expected since in the non-reduced model, there is a steep pressure gradient across the fault, where as in the reduced model, the pressure has a large discontinuity across the fracture. See Figs. 9a, b. However, a little far away from the fault the error is much smaller. The error in all the domain is of the order $\mathcal{O}\left(10^{-2}\right)$, confirming a good approximation in this case.

We chose as the permeability in the fault $\Lambda_f = \text{diag}\left\{1, 10^2\right\}$. Figure 10 shows the solutions obtained with the reduced model, Fig. 10a, with the full 2-D model on a refined mesh, Fig. 10b, and the error between them, Fig. 10c.

We note that the error in the strip around the fracture is not dominant as in the barrier case because the pressure is smoother; it changes more gradually across the fracture. For this problem, the error is half that of the previous case and is concentrated in the left part of the domain, since there the source term is larger. The solution is qualitatively the same.

We chose as the permeability in the fault $\Lambda_f = \text{diag}\left\{10^{-2}, 10^2\right\}$ if $25 \leq y \leq 75$ and Λ_f equal to the identity matrix otherwise, like in the subdomains. Figure 11 shows the solutions obtained with the reduced model, Fig. 11a, with the full 2-D model on a refined mesh, Fig. 11b. The behaviour of the error is a combination of the two previous cases. In fact, the larger error is concentrated close to the fault and decays away from it. Around the two extremities, the error behaves like in the last test case. The error is, however, of the same magnitude as for the first test case.

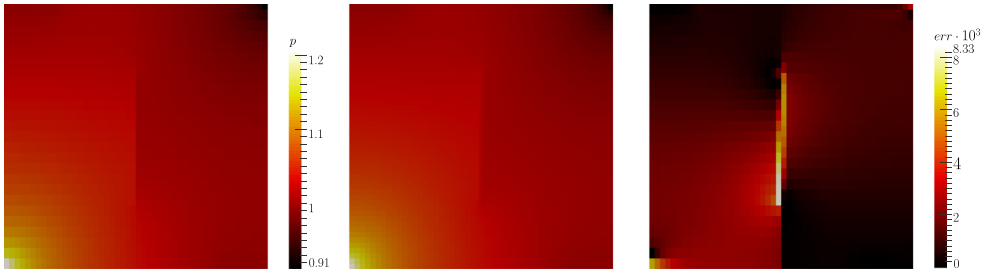

(a) With the *RM*. (b) Without the *RM*. (c) Model error.

Fig. 11 Fully immersed case: Model error between the reduced model solution on the coarse mesh (Fig 8b) and the full 2-D model solution on the fine mesh (Fig. 8c)

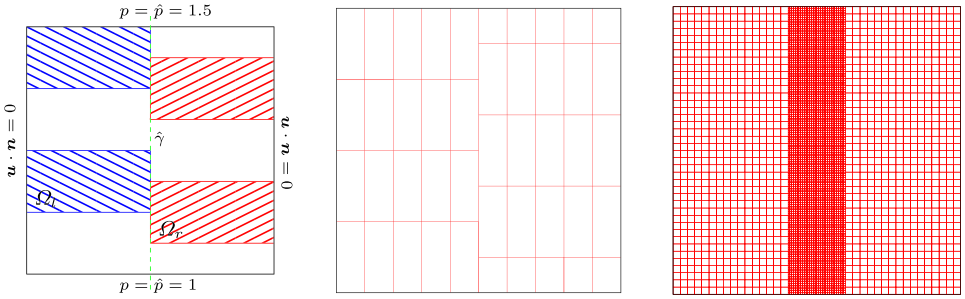

(a) Computational domain. (b) Coarse mesh. (c) Fine mesh.

Fig. 12 Heterogeneous academic case: **a** computational domain with some of the data and meshes. The coarse mesh **b** for the reduced model has 45 hexahedra outside the fault and 9 elements in the fault, while the fine mesh **c** corresponding to a fine 2-D discretization of the fault has 6400 hexahedra. In *blue* is depicted Ω_l and in *red* is depicted Ω_r

5.2 Model validity: heterogeneous problem

The following test case is inspired by the last example in [19]. We consider a problem with a heterogeneous porous medium composed by several layers and a fault in its middle. The domain and fault are

$$\Omega = (0, 100)^2 \text{ and } \hat{\gamma} = \left\{(x, y) \in \mathbb{R}^2 : x = 50\right\}$$

with fault thickness $d = 2.5$. We impose a zero source term and for pressure boundary conditions $p = 1.5$ on the top, and $p = 1$ on the bottom. Moreover, on the left and on the right, we impose a no flow boundary condition. The layers of the porous medium are defined as

$$\Omega_l = \left\{(x, y) \in \mathbb{R}^2 : y \in I_l \text{ and } x < 50\right\}$$
$$\Omega_r = \left\{(x, y) \in \mathbb{R}^2 : y \in I_r \text{ and } x > 50\right\},$$

where the intervals are defined as

$$I_l = [25, 50] \cup [75, 100] \quad \text{and}$$
$$I_r = [12.5, 37.5] \cup [62.5, 87.5].$$

A sketch of the computational domain is given in Fig. 12a. The permeability for the two layers are

$$\Lambda_l = \text{diag}\left\{10^{-3}, 10^{-3}\right\} \text{ in } \Omega_l,$$
$$\Lambda_r = \text{diag}\left\{10^{-2}, 10^{-2}\right\} \text{ in } \Omega_r$$

and $\Lambda = \boldsymbol{I}$ in $\Omega \setminus (\Omega_l \cup \Omega_r)$. Also, Fig. 12a shows two meshes, a non conforming coarse mesh which is used with the reduced model and a fine mesh corresponding to a fine 2-D discretization of the fault which is used for the full 2-D model.

For the permeability in the fault, we introduce the parameter $\zeta \in \mathbb{R}^+$ which is the ratio of the permeability in each layer of the fault to the permeability of the closer cell in the porous medium.

In Fig. 13, we present the solutions for the reduced model with the coarse mesh shown in Fig. 12b and for the full 2-D model with the fine mesh shown in Fig. 12c, for $\zeta = 10^{-2}$ and $\zeta = 10^4$.

For the case of a small value of ζ, i.e., the fault behaves as a barrier, we can see that the two solutions are similar qualitatively. When the fault behaves like a channel, i.e., $\zeta = 10^4$, we observe that all the small scales are lost near the fault and they are "homogenized" in a bigger cell. Anyway, the model error is still small in this case.

We performed some experiments varying ζ from 10^{-6} up to 10^{10}. We computed the error (32) for each value of ζ and we plotted the results in Fig. 14. We can see that the maximum of the error is very small for each value of ζ, even if we have an oscillation close to $\zeta = 10^{-1}$.

Moreover, we notice two different plateaus for ζ smaller than 10^{-5} and bigger than 10^5. We notice also that we commit at most an error lower than the 7 ‰, conforming that the method is quite robust despite the fact that the mesh in this test is really coarse.

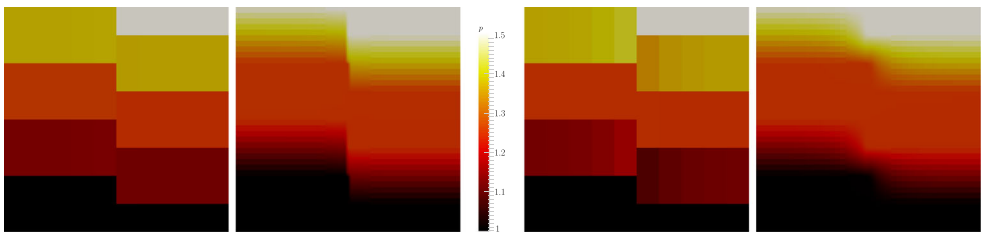

(a) With the RM. (b) Without the RM. $\zeta = 10^{-2}$ (c) With the RM. (d) Without the RM. $\zeta = 10^4$

Fig. 13 Heterogeneous academic case: reduced model solutions on the coarse mesh (Fig. 12b) and the full 2-D model solutions on the fine mesh (Fig. 12c) for two values of ζ.

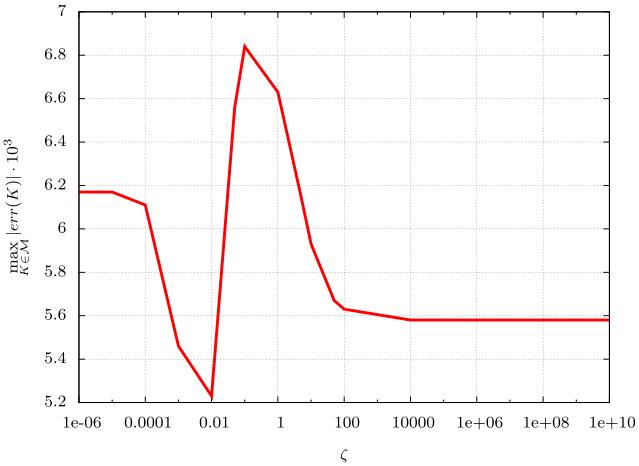

Fig. 14 Maximum of model error as a function of ζ

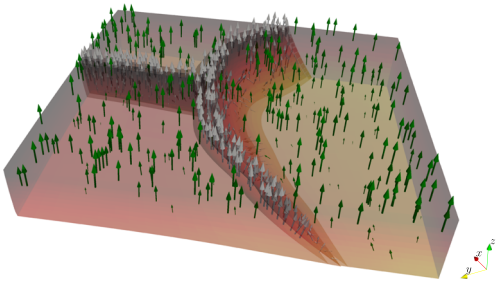

Fig. 16 Initial solution for the homogeneous case

5.3 A realistic experiment

For our final experiment, we consider a problem in a realistic setting. We consider the porous medium depicted in Fig. 15a with a T-shaped fault presented in Fig. 15b, c.

From these figures, we can see that the problem exhibits a geometrical non-conformity close to the fault. Unlike in the previous experiments, the faults here are not planar surfaces. This situation produces additional difficulties. Indeed, the two sides of a fault are non-matching, i.e., their topological structure differs, but also their geometric realization differ as they can have gaps in between each other due to the discretization. In particular, due to a precedent deposition and movement of the sedimentary layers, because of the fault, we have a different data distribution on the two sides of the fault. We will nonetheless employ the DLRM using appropriate projections to write the coupling conditions between the two sides of the fault. Moreover, some faces of the fault have only partial contact or even no contact with the other side of the fault. These faces or parts of faces are considered as boundary faces.

We have the following bounds for the computational domain $\Omega \subset (-1.37, 1.34) \cdot 10^4$ m$\times(-25.6, 1.73) \cdot 10^3$ m$\times(-4.11 \cdot 10^3, -75.2)$ m and a fault of thickness $d = 50$ m. We denote by $\partial\Omega^{\text{top}}$ the top part of the boundary, by $\partial\Omega^{\text{bott}}$ the bottom part of the boundary and by

$$\partial\Omega^{\text{rem}} = \partial\Omega \setminus (\partial\Omega^{\text{top}} \cup \partial\Omega^{\text{bott}})$$

the rest of the boundary. Also for this last example, we consider a problem slightly different from that of Eq. 1, a problem more closely related to those encountered in basin modeling in which flow is induced not by wells but by the compressibility of the porous medium thus leading to

Fig. 15 Representation of the domain and the fault grid for both layers. We can notice that the discretization is non-matching and we have a geometrical non-conformity. The color represents the different homogeneous strata

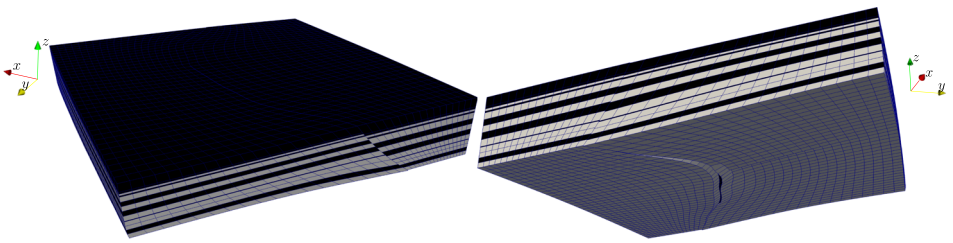

(a) Different views of the computational domain.

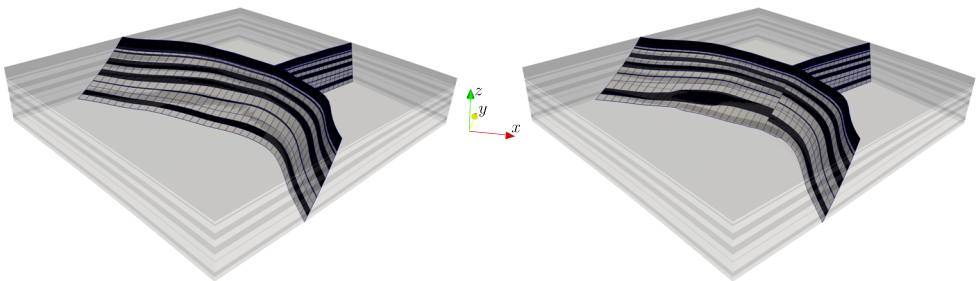

(b) Discretization of the first layer of the faults.

(c) Discretization of the second layer of the faults.

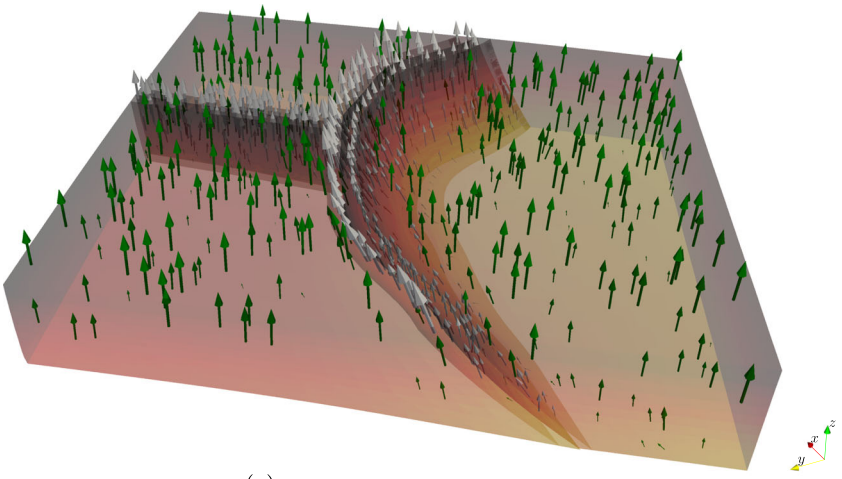

(a) The fault behaves like a barrier.

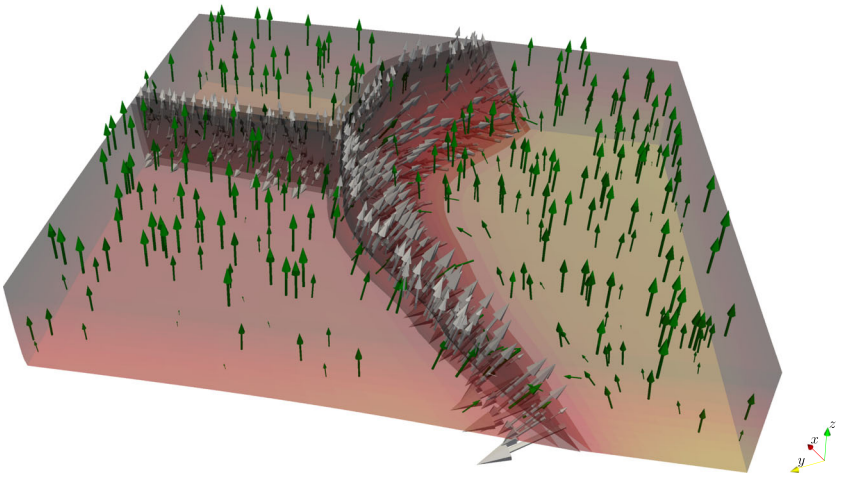

(b) The fault behaves like a channel.

Fig. 17 Solution for $t = 0.7$ My when the fault is a barrier or a channel for the flow

a parabolic equation for the pressure. Given t^* and T the initial and final times, we calculate p such that

$$\begin{aligned} &c\Phi\frac{\partial p}{\partial t} = \nabla\cdot\frac{\Lambda}{\mu}\nabla p && \text{in } \Omega\times(t^*,T),\\ &\Lambda\nabla p\cdot\boldsymbol{n} = 0 && \text{on } \partial\Omega^{\text{rem}}\times(t^*,T),\\ &p = 0 && \text{on } \partial\Omega^{\text{top}}\times(t^*,T),\\ &p = p_0 && \text{in } \Omega\times\{t^*\}, \end{aligned}$$

where $\mu = 3.1\cdot 10^4$ Pa· s is the dynamic viscosity, c is the compressibility, and Φ the porosity. Considering Fig. 15a, we impose $c\Phi = 0.2\cdot 10^{-4}$ Pa^{-1} in each of the black layer while $c\Phi = 10^{-4}$ Pa^{-1} in each of the white layer. The initial and final times are $t^* = 0y$ and $T = 2My$, respectively. The initial solution p_0 is the stationary solution of

$$\begin{aligned} &-\nabla\cdot\frac{\Lambda}{\mu}\nabla p_0 = 0 && \text{in } \Omega,\\ &\Lambda\nabla p_0\cdot\boldsymbol{n} = 0 && \text{on } \partial\Omega^{\text{rem}},\\ &\Lambda\nabla p_0\cdot\boldsymbol{n} = 0 && \text{on } \partial\Omega^{\text{bott}},\\ &p_0 = 0 && \text{on } \partial\Omega^{\text{top}},\\ &p_0 = 20 && \text{on } \partial\Omega^{\text{bott}}. \end{aligned}$$

For the computation of p_0, we consider the permeability in the fault cells equal to that of the surrounding domain cell, while for the bottom boundary condition of the fault we impose a zero flow condition. We use an implicit Euler scheme for the time discretization. The number of domain cells is 19,152, while the fault is discretized using 798 elements for each layer.

We consider different configurations of the problem corresponding to different values of the permeabilities of the porous medium and the fault. In the first case, we consider

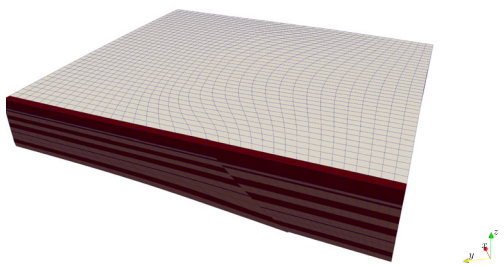

Fig. 18 Set of cells where we focus our attention

a homogeneous porous media with a permeability equal to $\Lambda = 10^{-17}\boldsymbol{I}\,\mathrm{m}^2$. In this case, we focus our attention on how the fault modifies the solution globally when we consider different values of its permeability.

Figure 16 shows the initial solution. As in the two following figures, we represent the Darcy solution with grey arrows in some of the cells close to the faults and with green arrows elsewhere. Since the permeability is constant we expect an almost linear solution for the pressure and a constant velocity. The solution respects the prevision.

We change now the permeability inside the fault considering two different scenarios, the fault is a barrier or

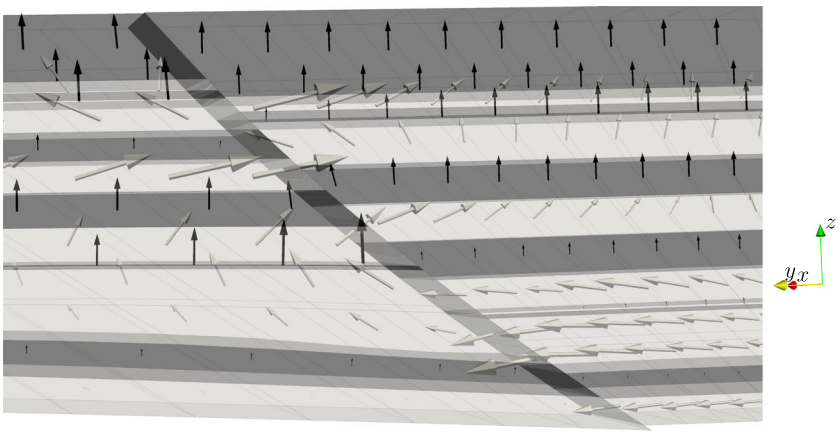

(a) The fault behaves like the surrounding medium.

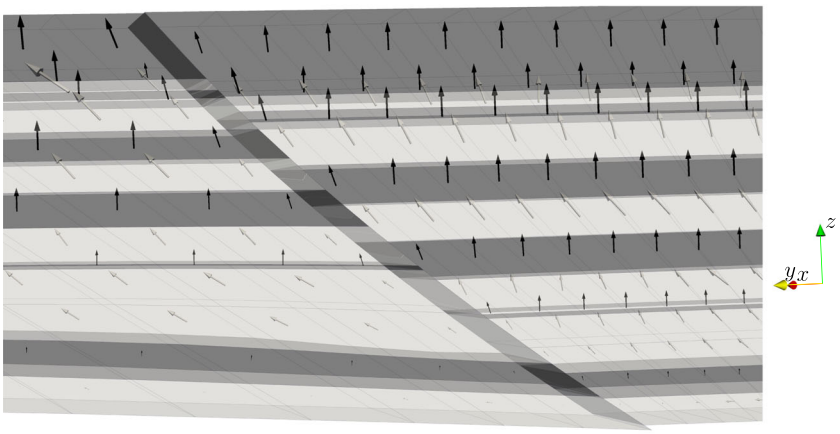

(b) The fault behaves like a barrier.

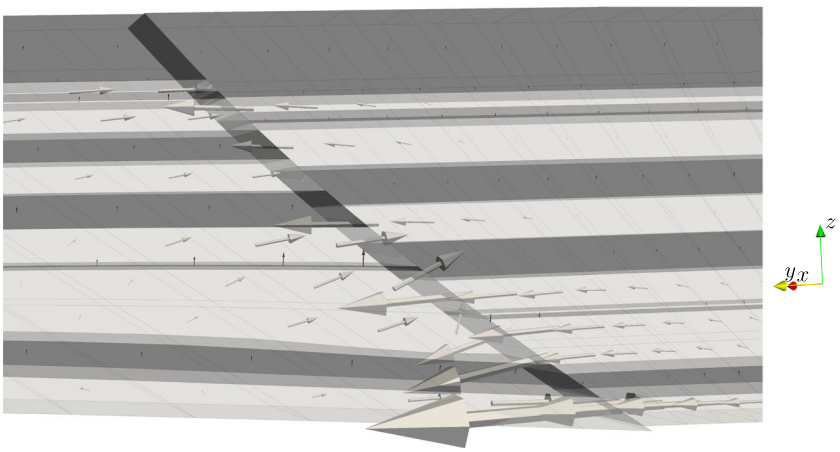

(c) The fault behaves like a channel.

Fig. 19 Solution for $t = 0.7$ My for different configurations of the fault. We use the same color for cells and arrows according to the cell permeability where the arrow origin is located, like in Fig. 15a. The scaling of the *arrows* in the three figures is different

Table 1 Average of the number of iterations for different configurations

Ω	$\hat{\gamma}$	ILU0
Homogeneous	Barrier	1
Homogeneous	Channel	3
Heterogeneous	Neutral	3
Heterogeneous	Barrier	2
Heterogeneous	Channel	5

the fault is a channel. In the first case, we impose a fault permeability $\Lambda_f = 10^{-19}\boldsymbol{I}\mathrm{m}^2$ while in the second case $\Lambda_f = 10^{-15}\boldsymbol{I}\mathrm{m}^2$.

In Fig. 17, we present the solution for both cases. In Fig. 17a, the fault clearly behaves like a barrier. Indeed, we do not see any arrow that cross the fault and the Darcy velocity tends to follow the fault geometry. Not very far from the fault, the flow is still vertical. The pressure has an almost linear shape from the bottom to the top of the domain. In the second case, reported in Fig. 17b, the fault behaves like a conductive channel for the flow of the surrounding domain. We clearly see that the flow of the closer cells, represented by the grey arrows, are directed to the fault since it is easier for the flow to move inside the fault than to stay outside. Some of the green arrows close to the fault are pointing to the fault since the influence of the fault is stronger than in the previous case. The pressure is smaller for the cells close to the fault than in the previous case.

We change now the permeability of the porous medium to analyze the interaction between the heterogeneities and the fault. Considering Fig. 15a, we impose as permeability in each of the black layer $\Lambda = 10^{-17}\boldsymbol{I}\mathrm{m}^2$ while in each of the white layer $\Lambda = 10^{-15}\boldsymbol{I}\mathrm{m}^2$. The black layers act as barriers while the latter are channels. We can notice that far from the fault the flow is almost upward, while close to the fault and thanks to the non uniform strata deposition the solution is complicated and not easily predictable. Since the solution is much more complex than in the previous cases, we focus our attention only on the red cells represented in Fig. 18.

Thanks to the different layers the flow can pass from one permeable layer to the other following the fault or the less permeable layers. We consider three different test cases changing the permeability in the fault. First of all, we impose the permeability in the fault cells equal to that the neighboring domain cell. In this case, the fault behaves like the surrounding part of the domain. Figure 19a represents the Darcy velocity only in the selected cells. In the bottom part of the domain, thanks to the fault, the flow can pass through the latter and starts to move upward in the more permeable strata. In the middle of the domain, since the barrier in the left part of the domain is thinner than in the right part, the flow is concentrated there. In the upper part of the domain the fluid moves from the left part to the right part and vice versa. In the second test case, represented in Fig. 19b, we consider the fault as a barrier imposing a small permeability $\Lambda_f = 10^{-19}\boldsymbol{I}\mathrm{m}^2$. We see that the arrows never cross the fault and the fluid moves only upward. Even considering the big black strata, the flow avoids to pass through the fault. The Darcy velocity of the cells close to the fault is parallel to the fault surface. The last test considers a fault that behaves like a channel. In fact, we impose $\Lambda_f = 10^{-13}\boldsymbol{I}\mathrm{m}^2$ as the permeability in the fault. Figure 19c shows the Darcy velocity for $t = 0.7$ My. The flow goes directly into the fault since the arrows are almost parallel to the layers and direct inward to the fault. Finally, the Darcy flow is stronger close the fault and larger at the bottom of the domain then at the top.

We have used an iterative scheme to solve the linear system. The algorithm chosen is the GMRES with tolerance on the stop criteria of 10^{-8} with ILU0 as preconditioner from PETSc library [7]. In Table 1 are reported the number of iterations for different configuration of the problem. We note that in all the case the preconditioner performs well.

6 Conclusion

In this paper, we have presented a novel approximation of the double-layer reduced model to describe the fault flows in a complex porous medium. The reduced model is a reasonable approximation when the thickness of a fault is some order of magnitude smaller than its other sizes. Moreover, the choice of the hybrid finite volume method allows us to handle, in a much robust and accurate way, different problem configurations. Particular attention is devoted to the analyses of the discrete equivalence that ease the implementation of the reduced model, for both the single-layer and double-layer model, avoiding to introduce the tangential operators and to approximate the coupling conditions. In the examples we have seen, the solution obtained with the reduced model compared to a reference solution in several situations. Finally, a real geometry with realistic data is presented to show the applicability of the reduced model to a real problem. The solution behaves as expected and no evidence of serious problems is seen.

Acknowledgments The authors warmly thank Jean-François Lecomte and Jean-Luc Rudkiewicz from IFP Energies nouvelles for constructing and providing the Eugene Island case from data in [40].

A Appendix

A.1 Nomenclature

We present the main nomenclature of this work. Some of the symbols are used only in one part of the domain, we use a subscript to indicate them. Some symbols for the numerical approximation can be found in Notation 1.

N Dimension of the domain
i Index $s.t.\ i \in \{1, 2, f\}$
j Index $s.t.\ j \in \{1, 2\}$
Ω Computational domain
Ω_f Fault domain
Ω_{f_j} Layer j of Ω_f
$\hat{\gamma}$ Fault centre
d Fault thickness
n Normal to $\hat{\gamma}$
T_j Normal thickness of Ω_{f_j}
p Pressure field
u Darcy velocity
Λ Permeability matrix
$\lambda_{f,n}$ Normal fault permeability
$\lambda_{f,\tau}$ Tangential fault permeability
q Source term
N Normal projection matrix
T Tangential projection matri
$\hat{p}$ Reduced pressure
$\hat{u}$ Reduced Darcy velocity
$\hat{\lambda}$ Reduced tangential permeability
$\lambda_{\hat{\gamma}}$ Reduced normal permeability
$\hat{q}$ Reduced source term
$\hat{u}_n$ Interface Darcy velocity normal to $\hat{\gamma}$
∇_τ Tangential gradient to $\hat{\gamma}$
$\nabla_\tau\cdot$ Tangential divergence to $\hat{\gamma}$
$\nabla_{\mathcal{D}}$ Discrete gradient
∇_K Discrete cell gradient
$R_{K,\sigma}$ Stabilization term for $\nabla_{\mathcal{D}}$
α Stabilization parameter
$\hat{\alpha}$ Reduced stabilization parameter
$[\![\cdot]\!]_\gamma$ Jump operator across γ
$\{\!\{\cdot\}\!\}_\gamma$ Mean operator across γ

A.2 TPFA and HFV schemes

The TPFA and HFV scheme are cell-centred finite volume schemes that gives an approximation of conductive fluxes on non-conforming grids. Theirs principle, using a finite volume philosophy, is briefly recalled in this section. A more detailed presentation can be found in [1, 16, 17]. The model problem is: find the unknown p such that

$$\begin{aligned} -\nabla\cdot\Lambda\nabla p &= q \quad \text{in } \Omega \\ p &= 0 \quad \text{on } \partial\Omega \end{aligned} \tag{33}$$

We consider the computational grid, approximation of Ω, defined as in Definition 1. Integrating (33) over each control volume $K \in \mathcal{M}$, gives the following

$$\sum_{\sigma\in\mathcal{E}_K}\int_\sigma \Lambda\nabla p\cdot\boldsymbol{n}_{K,\sigma}\mathrm{d}\sigma = \int_K q\mathrm{d}x \quad \forall K\in\mathcal{M}.$$

The flux $\int_\sigma \Lambda\nabla p\cdot\boldsymbol{n}_{K,\sigma}\mathrm{d}\sigma$ on each mesh edge $\sigma \in \mathcal{E}_K$ is approximated through a numerical flux function $F_{K,\sigma}(p)$ which depends only on the local unknowns related to K and $\mathcal{E}_K$. The discrete approximation of Eq. 33 is given by

$$\sum_{\sigma\in\mathcal{E}_K} F_{K,\sigma}(p) = \int_K q\mathrm{d}x \quad \forall K\in\mathcal{M}. \tag{34}$$

Since the previous system is defined cell-wise, we require the continuity of the flux on all the interior edges, imposing

$$F_{K,\sigma}(p) + F_{L,\sigma}(p) = 0 \quad \forall\sigma\in\mathcal{E}_{\text{int}} \tag{35}$$

with $\mathcal{M}_\sigma = \{K, L\}$.

A.2.1 TPFA scheme

To simplify the presentation, we require that $\Lambda(x) = \lambda(x)I$, with λ piece-wise constant on $\mathcal{M}$. We also assume that the discretization of Ω satisfies the superadmissible condition

$$\boldsymbol{n}_{K,\sigma} = (\boldsymbol{x}_\sigma - \boldsymbol{x}_K)/d_{K,\sigma} \quad \forall K\in\mathcal{M}, \forall\sigma\in\mathcal{E}_K \tag{36}$$

Then x_σ satisfies

$$\boldsymbol{x}_\sigma = \frac{d_{K,\sigma}\boldsymbol{x}_L + d_{L,\sigma}\boldsymbol{x}_K}{d_{K,\sigma}+d_{L,\sigma}} \text{ with } \mathcal{M}_\sigma = \{K, L\}, \tag{37}$$

The TPFA is constructed in the following way: if $\sigma \in \mathcal{E}_{\text{int}}$ with $\mathcal{M}_\sigma = \{K, L\}$, the approximate fluxes are given by

$$F_{K,\sigma}(p) = \lambda_K\,|\sigma|\,\frac{p_K - p_\sigma}{d_{K,\sigma}}$$
$$F_{L,\sigma}(p) = \lambda_L\,|\sigma|\,\frac{p_L - p_\sigma}{d_{L,\sigma}},$$

while if $\sigma \in \mathcal{E}_{\text{ext}}$ with $\mathcal{M}_\sigma = \{K\}$, the approximated flux is

$$F_{K,\sigma}(p) = \lambda_K\,|\sigma|\,\frac{p_K - p_\sigma}{d_{K,\sigma}}.$$

For each internal edge $\sigma \in \mathcal{E}_{\text{int}}$, imposing the continuity of the flux through it Eq. 35, it is possible to eliminate the

edge unknown p_σ and obtain the following expression for the discrete flux

$$F_{K,\sigma} = -F_{L,\sigma} = \begin{cases} \dfrac{\lambda_\sigma\,|\sigma|}{d_{K,\sigma}+d_{L,\sigma}}(p_K - p_L) & \text{if } \sigma \in \mathcal{E}_{\text{int}} \\ \dfrac{\lambda_K\,|\sigma|}{d_{K,\sigma}} p_K & \text{if } \sigma \in \mathcal{E}_{\text{ext}} \end{cases}$$

with

$$\lambda_\sigma = \frac{\lambda_K \lambda_L (d_{K,\sigma}+d_{L,\sigma})}{\lambda_K d_{L,\sigma} + \lambda_L d_{K,\sigma}}.$$

A.2.2 HFV scheme

To derive the HFV scheme, we express the Eqs. 34 and 35, introducing the test functions v constant for each cell $K \in \mathcal{M}$ as

$$\langle p, v\rangle_F = \sum_{K\in\mathcal{M}} v_K \int_K q\,\mathrm{d}x,$$

where the bilinear form is defined as

$$\langle p, v\rangle_F := \sum_{K\in\mathcal{M}} \sum_{\sigma\in\mathcal{E}_K} F_{K,\sigma}(p)\,(v_K - v_\sigma)\,.$$

The HFV scheme is based on a suitable choice of the discrete gradient $\nabla_{\mathcal{D}}\, p$, approximation of ∇p, such that the following relation holds true

$$\langle p, v\rangle_F = \sum_{K\in\mathcal{M}} (\Lambda \nabla_{\mathcal{D}}\, p, \nabla_{\mathcal{D}}\, v)_K\,.$$

The discrete gradient is chosen such that it is exact if the values of p correspond to a linear function and such that the bilinear form is coercive. Following [16, 17], we introduce the cell gradient

$$\nabla_K p := \frac{1}{|K|} \sum_{\sigma\in\mathcal{E}_K} |\sigma|\,(p_\sigma - p_K)\,\boldsymbol{n}_{K,\sigma}$$

and a stabilization term, defined in each cone of the cell (see Fig. 20), which is zero for linear functions and gives the definiteness property for the discrete bilinear form:

$$R_{K,\sigma}\, p := \frac{\beta}{d_{K,\sigma}}\,[p_\sigma - p_K - \nabla_K p\cdot(\boldsymbol{x}_\sigma - \boldsymbol{x}_K)]\,,$$

with $\beta = \alpha\sqrt{N}$ and α a stabilization parameter which can vary between each cell. The stabilization parameter $\alpha > 0$ is used to ensure coercivity of the discrete bilinear form. If $R_{K,\sigma}$ is not considered, the cell unknowns are not uniquely defined and the corresponding linear system is singular. Finally, the discrete gradient $\nabla_{\mathcal{D}}\, p$ is defined for each cone $D_{K,\sigma} \subset K$ as

$$\nabla_{\mathcal{D}}\, p|_{D_{K,\sigma}} := \nabla_K p + R_{K,\sigma}\, p \boldsymbol{n}_{K,\sigma}.$$

It is shown that then, the bilinear form writes

$$\langle p, v\rangle_F = \sum_{K\in\mathcal{M}} |K|\,\Lambda_K \nabla_K p\cdot\nabla_K v + \tag{38}$$
$$+ \sum_{\sigma\in\mathcal{E}_K} \alpha^2 \frac{|\sigma|\,d_{K,\sigma}}{d} R_{K,\sigma}\, p R_{K,\sigma}\, v \boldsymbol{n}_{K,\sigma}\cdot\Lambda_K \boldsymbol{n}_{K,\sigma}$$

It can be derived also a closed form for the discrete flux $F_{K,\sigma}$, which can be expressed as

$$F_{K,\sigma}(p) = \sum_{\sigma'\in\mathcal{E}_K} A_K^{\sigma\sigma'}\,(p_K - p_{\sigma'})\,,$$

with $(A_K^{\sigma\sigma'})_{\sigma\sigma'\in\mathcal{E}_K}$ a local symmetric and positive matrix. Its expression can be found in [17].

Remark 4 It is straightforward to extend the HFV scheme to the case of non-conforming grids. Instead of considering edges of the mesh, we consider sub-edges which are intersections of edges of different cells, and then for the construction of the discrete gradient the cones are built based on the sub-edges. An example is shown in Fig. 20.

Remark 5 If the discretization fulfills the superadmissible condition (36) and the centre of the edges is chosen as in Eq. 37 and moreover if the permeability is such that $\Lambda(x) = \lambda(x)I$, with λ piece-wise constant on $\mathcal{M}$ then, from Lemma 2.1 of [17], the HFV scheme with $\alpha = 1$ is equivalent to the TPFA presented in Section 6.

Remark 6 An extension, presented in [14], of the HFV scheme considers a stabilization parameter that is no longer

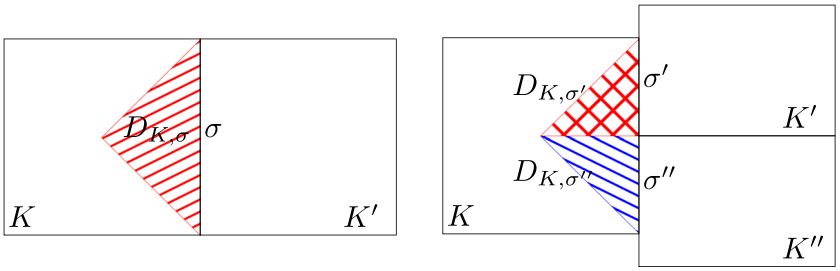

(a) Matching cells (b) Non-matching cells

Fig. 20 Representation of the subdivision in cones for a matching pair of cells and for non-matching cells

a scalar but a matrix. The stabilization term in Eq. 38 becomes

$$\sum_{K\in\mathcal{M}}\sum_{\sigma,\sigma'\in\mathcal{E}_K} B_{K,\sigma,\sigma'} S_{K,\sigma} p S_{K,\sigma'} v,$$

with $\left(B_{K,\sigma,\sigma'}\right)_{\sigma,\sigma'\in\mathcal{E}_K}$ a symmetric and positive matrix for the cell $K \in \mathcal{M}$ and

$$S_{K,\sigma} p := p_\sigma - p_K - \nabla_K p \cdot (\boldsymbol{x}_\sigma - \boldsymbol{x}_K)\,.$$

References

1. Aavatsmark, I.: Interpretation of a two-point flux stencil for skew parallelogram grids. Comput. Geosci. **11**(3), 199–206 (2007)
2. Pierre, M.A., Thovert, J.-F.: Fractures and fracture networks. Springer (1999)
3. Adler, P.M., Thovert, J.-F., Valeri, V.: Mourzenko. Fractured porous media. Oxford University Press (2012)
4. Alboin, C., Jaffré, J., Roberts, J.E., Wang, X., Serres, C.: Domain decomposition for some transmission problems in flow in porous media, volume 552 of Lecture Notes in Physics, pp. 22–34. Springer, Berlin (2000)
5. Angot, P., Boyer, F., Hubert, F.: Asymptotic and numerical modelling of flows in fractured porous media. M2AN Math. Model. Numer. Anal. **43**(2), 239–275 (2009)
6. Baca, R.G., Arnett, R.C., Langford, D.W.: Modelling fluid flow in fractured-porous rock masses by finite-element techniques. Int. J. Numer. Methods Fluids **4**(4), 337–348 (1984)
7. Balay, S., Brown, J., Buschelman, K., Eijkhout, V., Gropp, W.D., Kaushik, D., Knepley, MG., McInnes, L.C., Smith, BF., Zhang, H.: PETSc users manual. Technical Report ANL-95/11 - Revision 3.4, Argonne National Laboratory (2013)
8. Bear, J., Tsang, C.-F., de Marsily, G.: Flow and contaminant transport in fractured rock. Academic Press, San Diego (1993)
9. Berkowitz, B.: Characterizing flow and transport in fractured geological media: a review. Adv. Water Resour. **25**(8–12), 861–884 (2002)
10. Biryukov, D., Kuchuk, F.J.: Transient pressure behavior of reservoirs with discrete conductive faults and fractures. Trans. Porous Med. **95**(1), 239–268 (2012)
11. Brenner, K., Groza, M., Guichard, C., Masson, R.: Vertex approximate gradient scheme for hybrid dimensional two-phase darcy flows in fractured porous media. ESAIM: Math. Modell. Numer. Anal. **49**(2), 303–330 (2015)
12. Brezzi, F., Fortin, M.: Mixed and Hybrid Finite Element Methods, volume 15 of *Computational Mathematics*. Springer Verlag, Berlin (1991)
13. D'Angelo, C., Scotti, A.: A mixed finite element method for Darcy flow in fractured porous media with non-matching grids. Math. Modell. Numer. Anal. **46**(02), 465–489 (2012)
14. Droniou, J., Eymard, R., Gallouët, T., Herbin, R.: A unified approach to mimetic finite difference, hybird finite volume and mixed finite volume methods. Math. Models Methods Appl. Sci. **20**(02), 265–295 (2010)
15. Ern, A., Guermond, J.-L.: Theory and practice of finite elements. Springer (2004)
16. Eymard, R., Gallouët, T., Herbin, R.: A new finite volume scheme for anisotropic diffusion problems on general grids: convergence analysis. Compt. Rendus Math. **344**(6), 403–406 (2007)
17. Eymard, R., Gallout, T., Herbin, R.: Discretization of heterogeneous and anisotropic diffusion problems on general nonconforming meshes sushi: a scheme using stabilization and hybrid interfaces. IMA J. Numer. Anal. **30**(4), 1009–1043 (2010)
18. Faille, I., Flauraud, E., Nataf, F., Pégaz-Fiornet, S., Schneider, F., Willien, F.: A new fault model in geological basin modelling, Application of finite volume scheme and domain decomposition methods. In: Finite volumes for complex applications, III (Porquerolles, 2002), pp. 529–536. Hermes Scientific Publications, Paris (2002)
19. Faille, I., Nataf, F., Saas, L., Willien, F.: Finite Volume Methods on Non-Matching Grids with Arbitrary Interface Conditions and Highly Heterogeneous Media. In: Barth, T.J., Griebel, M., Keyes, D.E., Nieminen, R.M., Roose, D., Schlick, T., Kornhuber, R., Hoppe, R., Priaux, J., Pironneau, O., Widlund, O., Xu, J. (eds.) Domain Decomposition Methods in Science and Engineering, volume 40 of Lecture Notes in Computational Science and Engineering, pp. 243–250. Springer Berlin Heidelberg (2005)
20. Formaggia, L., Fumagalli, A., Scotti, A., Ruffo, P.: A reduced model for Darcy's problem in networks of fractures. ESAIM: Math. Modell. Numer. Anal. **48**, 7 (2014)
21. Frih, N., Martin, V., Roberts, J.E., Ai, S.: Modeling fractures as interfaces with nonmatching grids. Comput. Geosci. **16**(4), 1043–1060 (2012)
22. Frih, N., Roberts, J.E., Saada, A.: Modeling fractures as interfaces: a model for Forchheimer fractures. Comput. Geosci. **12**(1), 91–104 (2008)
23. Fumagalli, A., Scotti, A.: A numerical method for two-phase flow in fractured porous media with non-matching grids. Adv. Water Resour. **62**(Part C(0)), 454–464 (2013). Computational Methods in Geologic CO2 Sequestration
24. Fumagalli, A., Scotti, A.: An efficient xfem approximation of darcy flow in arbitrarly fractured porous media. Oil Gas Sci. Technol. - Revue d'IFP Energ. Nouvelles **69**(4), 555–564 (2014)
25. Hægland, H., Assteerawatt, A., Dahle, H.K., Eigestad, G.T., Helmig, R.: Comparison of cell- and vertex-centered discretization methods for flow in a two-dimensional discrete-fracture-matrix system. Adv. Water Resour. **32**(12), 1740–1755 (2009)
26. Herbin, R., Hubert, F., et al.: Benchmark on discretization schemes for anisotropic diffusion problems on general grids. Finite volumes for complex applications V, 659–692 (2008)
27. Hoteit, H., Firoozabadi, A.: Multicomponent fluid flow by discontinuous galerkin and mixed methods in unfractured and fractured media. Water Resour. Res. **41**(11) (2005)
28. Hoteit, H., Firoozabadi, A.: An efficient numerical model for incompressible two-phase flow in fractured media. Adv. Water Resour. **31**(6), 891–905 (2008)
29. Huang, H., Long, T.A., Wan, J., Brown, W.P.: On the use of enriched finite element method to model subsurface features in porous media flow problems. Comput. Geosci. **15**(4), 721–736 (2011)
30. Jaffré, J., Mnejja, M., Roberts, J.E.: A discrete fracture model for two-phase flow with matrix-fracture interaction. Proced. Comput. Sci. **4**, 967–973 (2011)
31. Karimi-Fard, M., Durlofsky, L.J., Aziz, K.: An efficient discrete-fracture model applicable for general-purpose reservoir simulators. SPE J. **9**(2), 227–236 (2004)
32. Karimi-Fard, M., Firoozabadi, A.: Numerical simulation of water injection in fractured media using the discrete-fracture model and the galerkin method. SPE Reserv. Eval. Eng. **6**(2), 117–126 (2003)

33. Knabner, P., Jean, E.: Roberts. Mathematical analysis of a discrete fracture model coupling Darcy flow in the matrix with darcy-forchheimer flow in the fracture. 48 **9**, 1451–1472 (2014)
34. Martin, V., Jaffré, J., Roberts, J.E.: Modeling fractures and barriers as interfaces for flow in porous media. SIAM J. Sci. Comput. **26**(5), 1667–1691 (2005)
35. Monteguado, J.E.P., Firoozabadi, A.: Control-volume method for numerical simulation of two-phase immiscible flow in two- and three-dimensional discrete-fractured media. Water Resour. Res. **40**(7), n/a–n/a (2004)
36. Morales, F., Showalter, R.E.: The narrow fracture approximation by channeled flow. J. Math. Anal. Appl. **365**(1), 320–331 (2010)
37. Morales, F., Showalter, R.E.: Interface approximation of Darcy flow in a narrow channel. Math. Methods Appl. Sci. **35**(2), 182–195 (2012)
38. Quarteroni, A., Valli, A.: Numerical approximation of partial differential equations, volume 23 of Springer Series in Computational Mathematics. Springer-Verlag, Berlin (1994)
39. Reichenberger, V., Jakobs, H., Bastian, P., Helmig, R.: A mixed-dimensional finite volume method for two-phase flow in fractured porous media. Adv. Water Resour. **29**(7), 1020–1036 (2006)
40. Revil, A., Cathles, L.M., III: Fluid transport by solitary waves along growing faults a field example from the south eugene island basin, gulf of Mexico. Earth and Planetary Science Letters, 321–335 (2002)
41. Roberts, J.E., Thomas, J.-M.: Mixed and hybrid methods. In: Handbook of numerical analysis, vol. II, pp. 523–639. North-Holland, Amsterdam (1991)
42. Tunc, X., Faille, I., Gallouët, T., Cacas, M.C., Havé, P.: A model for conductive faults with non-matching grids. Comput. Geosci. **16**, 277–296 (2012)